Proceedings of the Workshop

"Gamma-Ray Bursts: Probing the Science, Progenitors and their Environment"

Moscow, 13 - 15 June 2012

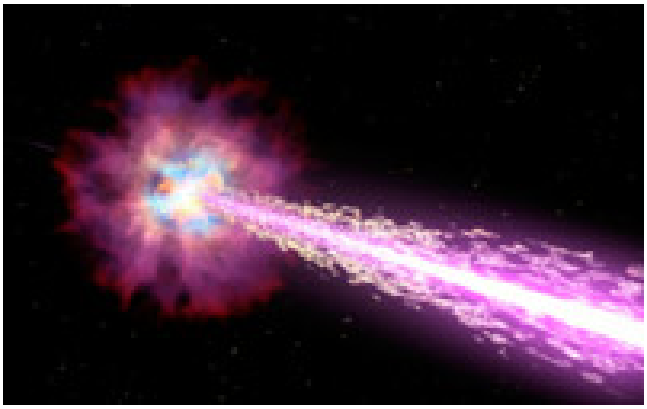

Extreme Universe Laboratory
Skobeltsyn Institute of Nuclear Physics
Lomonosov Moscow State University

1(2), Leninskie gory, GSP-1, Moscow 119991, Russian Federation

Contents

Gamma ray bursts, their afterglows, and soft gamma repeaters

G.S. Bisnovatyi-Kogan
Space Research Institute (IKI), Russian Academy of Sciences, 117997, 84/32 Profsoyuznaya Str, Moscow, Russian Federation

Abstract

The conclusion, that cosmic γ-ray bursts (GRBs) are of cosmological origin, is based on the statistical analysis of GRBs and the measurements of line redshifts in GRB optical afterglows. In most of these models, if not in all of them, the isotropic radiation cannot provide the energy release necessary for the appearance of a cosmological GRB. Observations of bright optical GRB afterglows point to the fact that an initially bright optical flare is directly related to the GRB itself, and the subsequent weak and much more continuous optical radiation is of a different nature. The interaction of the cosmological GRB radiation with a dense surrounding molecular cloud results in the appearance of long-duration (up to 10 years) weak optical afterglows associated with the heating and reradiation of gas. Results of 2D numerical simulation of the heating and reradiation of gas in various variants of the relative disposition of GRB and molecular clouds are presented. The possible relation between the short GRBs and soft gamma repeaters (SGR) is discussed. The model of SGR activity, based on nuclear explosion in the nonequilibrium layer in the neutron star crust, is discussed.

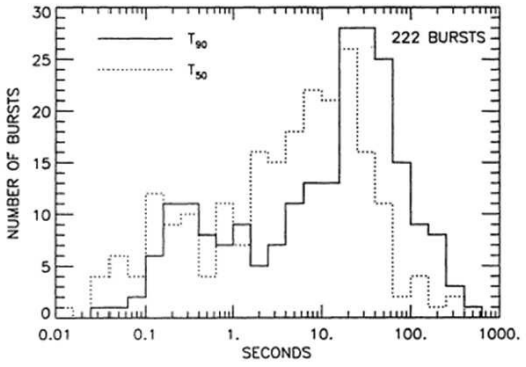

Figure 1: Duration of 222 GRB from BATSE catalog, [5].

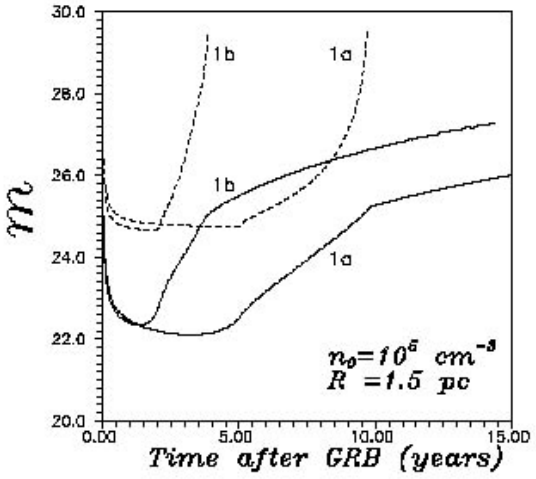

Figure 2: The light curve of the optical afterglow, in stellar magnitudes Maximal expected - hard line, minimal expected - dash line. Time zero corresponds to the GRB outburst with with the gamma energy E, and the total flux near the Earth $F_{\rm GRB} = 10^{-4}$ erg cm^{-2}: 1a. - for the case $E = 10^{52}$ erg; $n_0 = 10^5$ cm^{-3}; 1b - for the case $E = 10^{51}$ erg; $n_0 = 10^5$ cm^{-3}, [2]

1 Energy sources

It is accepted now that cosmic γ-ray bursts (GRBs), reported in 1973 [1], are of cosmological origin. The key problem is associated with searching for the possibility of an enormous, $(10^{51} - 10^{54}$ erg energy release (for isotropic burst radiation) over a short (0.1–100 s) time. From the various proposed models, the following ones are discussed more frequently.

(i) *The coalescence of two neutron stars or a neutron star and a black hole of a stellar mass.*

(ii) *Magnetorotational explosion.*

(iii) *Hypernova.*

(iv) *Magnetized disk around a (Kerr) rotating black hole (RBH).* This model is based on extracting the RBH rotation energy for the GRB production, due to its magnetic coupling with the RBH and the surrounding accretion disk or torus. GRB has difference duration and are divided in long and short events (Fig.1) GRB are observed at high redshifts, up to $z \sim 8.2$, (GRB 090423). GRB-SN connections is found only for long GRB.

1.1 Afterglows

The optical afterglows had been first observed after the satellite Beppo-SAX identification. The model of the afterglow is not well established, and several mechanisms are proposed, even for the same GRB. The prompt optical emission is produced by the mechanism, different from the later, and much weaker optical transient (GRB080319). If GRB is surrounded by a dense gas cloud, the optical afterglow appeared as absorbtion of gamma quanta, and reradiation in the optical band. The 1-D calculations have been done in [2] in spherically symmet-

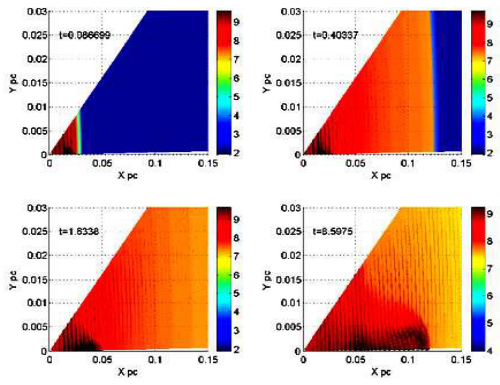

Figure 3: Flow velocity (arrows) and temperature (color fill) of the matter at various times for strongly anisotropic cloud with total GRB energy $\approx 2 \cdot 10^{53}$ erg. The distance from the GRB source is given in parsecs, and the indicated times are in years since the GRB. The right-hand bars give the log T(K) temperature scale, [3]

ric model (Fig.2), 2D calculations are done in [3], where duration and beaming depend strongly on the geometry and density distribution in the cloud (Fig.3). Reradiation of the gamma ray flux by a dusty cloud may lead to appearance of the infrared afterglow, observed in GRB041219, without optics [4].

2 Prompt optical emission

Figure 4: Camera FAVOR - NIIPP, SAO, IKI.

Bright optical afterglow was observed in a long GRB990123, which lasted ~ 100 s, with T(50%)=30 s, and T(90%)=63 s.The burst was observed by the instruments BATSE, KONUS, ASCA; OSSE, with $E_\gamma < 10$ MeV, COMPTEL with the range 0.2–30 MeV on the board of COMPTON observatory. After the burst localization by Beppo-SAX, the optical observations of the afterglow was done by ROTSE in Los Alamos, started at $t = 22.18$ s after beginning of GRB, in unfiltered light. At January 24, this GRB was observed for 40 min by the KECK telescope, obtaining the optical spectrum showing the redshift z=1.61. The total energy (isotropic) of GRB was as follows: $Q_\gamma > 2.3 \cdot 10^{54}$ erg. The optical luminosity was equal to $L_{opt} > 2 \cdot 10^{16}\, L_\odot \approx 8 \cdot 10^{49}$ erg/s. Weaker prompt optical emission was observed also in GRB 021004 (15m, z=2.3), GRB 030329 (12.4m, z=0.168), and GRB 030418 (16.9m). A new strategy of the optical afterglow search was realized by Pozanenko et al. [6]. The wide field of view 400-600 sq. grad camera, with time resolution 0.13 sec, and limiting magnitude 10m 11.5m, was installed in SAO (Russia), see fig.4, and later in La Silla (Chile), see fig.5. Amount of data is ~ 600 Gb/night. The most exciting GRB afterglow was observed in GRB080319 by Tortora camera in La Silla. Due to very wide field of view the region of this GRB was observed during whole time of the burst, during the whole prompt emission phase [7], Fig.6, simultaneously with gamma ray observations made by BATSE and KONUS instruments. The KONUS light curve is given in Fig.7.

Evidently, the prompt optical emission, during one minute of GRB flash, is strongly correlated with the gamma ray light curve. It may indicate to the same level of collimation in prompt optical emission, as in gamma radiation. Optical afterglows (at longer times) probably are not collimated. This is important for estimation of the frequency of the "naked" optical flashes, which may be observed in absence of gamma radiation, due to absence of a collimation. It follows, that we may expect only weak flashes from uncollimated optics.

Figure 5: TORTOREM = Tortora + REM, La Silla, In automatic regime since May, 2006.

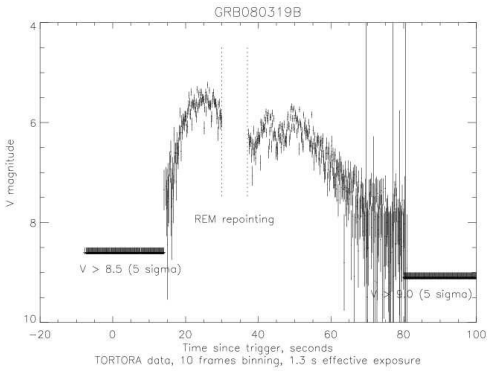

Figure 6: from [7], http://vo.astronet.ru/∼karpov/grb080319b_lc_10.gif

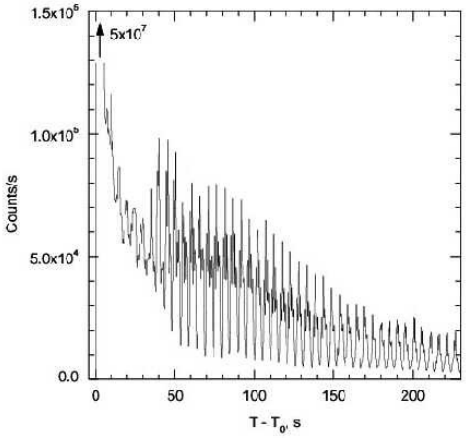

Figure 8: The giant 1998 August 27 outburst of the soft gamma repeater SGR 1900 + 14, from [9].

3 Soft gamma repeators (SGR)

SGR are neutron stars with periods (until recently) P= 5 8 seconds. They are characterized by a strong variability, with long intervals of low luminosity, and appearance of giant bursts, in which a peak luminosity increase 5 6 orders of magnitude. Slow rotation, low rotational energy, imply a low rotational energy losses, so that observed average luminosity exceeds rotational loss of energy more than 10 times, and many orders of magnitude during giant outbursts Suggestion was done, that the source of energy is an annihilation of a very strong magnetic field of a neutron star, and these sources are "magnetars". Regular pulsations are clearly visible in fig.8, during giant bursts [9]. Giant bursts in SGR are similar to short GRB [11, 12]. Short GRB, interpreted as giant bursts of SGR were observed in M31 (Andromeda) [13], and in M81 [14].

4 SGR - magnetars ?

Long periods and strong magnetic fields should explain, why magnetars are very different from radiopulsars, but several opposite examples were observed. A radio pulsar with an 8.5-second period was reported in [15]. Several radiopulsars have very large magnetic fields, like the hypothetical magnetars. PSR J1119-6127 has a period P=0.407 s, and the magnetic field strength of $B = 4.1 \cdot 10^{13}$ G. The pulsar, PSR J1814-1744, has P=3.975 s and $B = 5.5 \cdot 10^{13}$ G [16]. Another two pulsars with "magnetar"-like magnetic field were reported in [17]: PSR J1847-013, with P=6.7 s., and $B = 9.4 \cdot 10^{13}$ G, and PSR J1718-37, with P=3.4 s., and $B = 7.4 \cdot 10^{13}$ G. Important discovery was done by observations of SGR/AXP 1E1550.0-5418, where small period of rotation P= 2.1 s. was found [18]. Finally, it was reported 19 on a SGR 0418+5729 with low magnetic field, recently detected after it emitted bursts similar to those of magnetars. X-ray observations show that its dipolar magnetic field cannot be greater than $7.5 \cdot 10^{12}$ Gauss, well in the range of ordinary radio pulsars. That indicates that a high surface dipolar magnetic field is not necessarily required for magnetar-like activity.

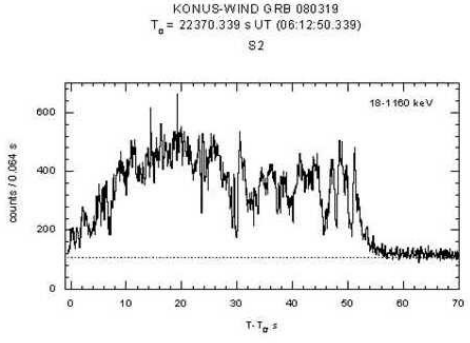

Figure 7: from [8], http://www.ioffe.rssi.ru/LEA/GRBs/GRB080319_T22370/

5 Nuclear explosion model of SGR activity

It was shown in[20], that neutron stars crust consist of the elements far from nuclear equilibrium. By estimations [20] in the most heavy neutron stars nonequilibrium layer mass is $\sim 2 \cdot 10^{29}$ g=$10^{-4} M_{\odot}$. In smaller mass neutron stars this layer is more massive. For M=0.45 the mass of the nonequilibrium layer is 7 times larger, fig.10. The energy store reaches 10^{49} erg, what is enough for $\sim$ 1000 giant bursts [21]. The nuclear explosion was suggested as GRB model in previous times, when they were related to the galactic origin [22]. Presently only SGR remain the objects, where a violent activity may be connected with nuclear explosions, related to the crust breaks.

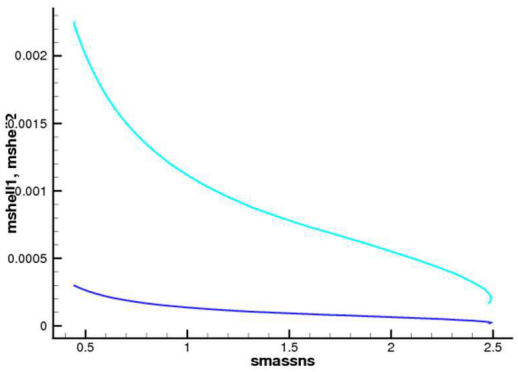

Figure 9: The mass of nonequilibrium layer as a function of NS mass, from [22].

6 Conclusions

Conclusions GRB cosmological objects of unknown nature (BH+heavy magnetized disk ?) The key information may be coded in the prompt optical afterglow (polarization, spectra) 3. SGR highly active, slowly rotating neutron stars 4. Nonequilibrium layer is formed in the neutron star crust, during NS cooling, or during accretion onto it. It may be important for NS cooling, glitches, and explosions connected with SGR 5. The mass and the energy store in NL increase rapidly with decreasing NS mass 6. NL in low mass NS may be responsible for explosions, producing SGR

Acknowledgments

This was partially supported by RFBR grant 11-02-00602, the RAN Program Formation and evolution of stars and galaxies and Russian Federation President Grant NSh-3458.2010.2.

References

[1] Klebesadel R. W., Strong I. B. & Olson R. A., Astrophys. J. Lett. **,**, 182 (L85)1973.

[2] Bisnovatyi-Kogan G. S. & Timokhin A. N., Sov. Astron. **,**, 41 (423)1997.

[3] Barkov M.V., Bisnovatyi-Kogan G. S., Astron.Rep. **,**, 49 (24)2005.

[4] Barkov M.V., Bisnovatyi-Kogan G. S., Astrophysics **48**, 369 (2005).

[5] Fishman G. J., Meegan C. A., Ann. Rev. Astron. Ap. **33**, 415 (1995).

[6] Pozanenko A., Chernenko A., Beskin G., et al. Astron. Data Analysis Software and Systems. XII ASP Conf. Series, Vol. 295, p. 457, 2003. H. E. Payne, R. I. Jedrzejewski, and R. N. Hook, eds.

[7] Karpov S., Beskin G., Bondar S., et al. GRB Coordinates Network, Circular Service, 7558, 1 (2008).

[8] Golenetskii S., Aptekar R., Mazets E., et al. GRB Coordinates Network, Circular Service, 7482, 1 (2008).

[9] Mazets E.P., Cline T.L., Aptekar' R.L., et al. Astron. Lett. **25**, 635 (1999).

[10] Mazets E.P., Cline T.L., Aptekar' R.L., et al. eprint arXiv:astro-ph/0502541, 02/2005.

[11] Bisnovatyi-Kogan G. Mem. Soc. Astron. It. **73**, 318 (2002), astro-ph/9911275.

[12] Mazets E.P., Cline T.L., Aptekar' R.L. Astron. Lett. **25**, 628 (1999).

[13] Mazets E.P., Aptekar R.L., Cline T.L., et al. ApJ **680**, 545 (2008).

[14] Frederiks D.D., Palshin V.D., Aptekar R.L., at al. Astron. Lett. **33**, 19 (2007).

[15] Young M.D., Manchester R.N., Johnston S. Nature **400**, 848 (1999).

[16] Camilo F., Kaspi V.M., Lyne A.G., et al. ApJ **541**, 367 (2000).

[17] McLaughlin M.A., Lorimer D.R., Lyne A.G., et al. ASP Conference Series, Vol. 218, p.255 (2004). Proc. IAU Symp. "Young Neutron Stars and Their Environments", July, 2003, Sydney, Australia. Eds. F. Camilo and B.M. Gaensler.

[18] Kuiper L., den Hartog P.R., Hermsen W. The Astronomer's Telegram, 1921, 01/2009.

[19] Rea N., Esposito P., Turolla R., et al. Science **330**, 944 (2010), arXiv:1010.2781.

[20] Bisnovatyi-Kogan G.S., Chechetkin V.M. ApSS **26**, 25 (1974).

[21] Bisnovatyi-Kogan, G. S, Tarasov S.O. (2012), in preparation.

[22] Bisnovatyi-Kogan G.S., Imshennik V.S., Nadyozhin D.K., Chechetkin V.M. ApSS **35**, 23 (1975).

[23] Bisnovatyi-Kogan G.S In: Gamma-ray bursts - Observations, analyses and theories (A93-20206 06-90), p. 89-98 (1992).

Gamma-ray spectrometer BDRG onboard "Lomonosov": design, characteristics and test results

V.V. Bogomolov, S.I. Svertilov, N.N. Vedenkin, A.M. Amelushkin, G.F. Smoot
Extreme Universe Laboratory, Skobeltsyn Institute of Nuclear Physics, Lomonosov Moscow State University, 1(2), Leninskie gory, GSP-1, Moscow 119234, Russian Federation

Abstract

BDRG gamma-ray spectrometer for "Lomonosov" mission is designed to obtain temporal and spectral information about GRBs in the energy range 10-3000 keV as well as to produce GRB trigger at several time scales (20 ms, 1 s and 20 s). BDRG instrument consists of 3 identical detector boxes with axes shifted by 90° from each other. Such design allows to provide coordinates of GRB sources with an accuracy of $\sim 2°$. Each BDRG box is a phosvich NaI(Tl)/CsJ(Tl) scintillator detector. A considerably thick CsI(Tl) crystal ($\oslash$ 130 × 17 mm) placed behind NaI(Tl) is used as an active shield in the soft energy range and as the main detector in the hard one. The ratio between the rates of NaI(Tl) and CsI(Tl) events with different energy release can be used as a self-criterion for separation of real GRB events and their imitations by near-Earth electrons. The data from 3 detectors are collected in the BA BDRG information box producing GRB trigger and forming a set of output data frames. The daily amount of scientific data ($\sim$ 100 Mb) contains a continuous part of $\sim$ 35 Mb (1 s timing in 16 channels, detailed energy spectra) and sets of frames with detailed information for burst-like events ($\sim$ 2 Mb for a burst). A number of tests provided with BDRG confirmed its reliability, calibration and trigger production algorithm.

1 The GRB complex onboard the "Lomonosov" mission

The scientific program of the "Lomonosov" space mission includes a multi-wavelength GRB study at different time scales. In particular, the complex study of prompt emission will be provided based on the direct recording of readings of wide field optical cameras as well as on the fast pointing of optical and UV telescope using its moving mirror. The spacecraft "Lomonosov" will contain 3 instruments for GRB study: gamma-ray spectrometer BDRG, a wide field optical camera SHOK, and a complex of coding mask X-ray telescope and UV telescope named UFFO.

BDRG gamma-ray spectrometer for the "Lomonosov" mission is designed to obtain temporal and spectral information about GRBs in the energy range 10-3000 keV as well as to produce GRB triggers. The trigger will be used onboard to fix some amount of history data stored in the internal memory of all instruments of the GRB complex as well as to start the detailed data collection. Within some delay, the position of the GRB will be estimated and the telegram with trigger information will be sent to the world GRB net via Global Star transmitter.

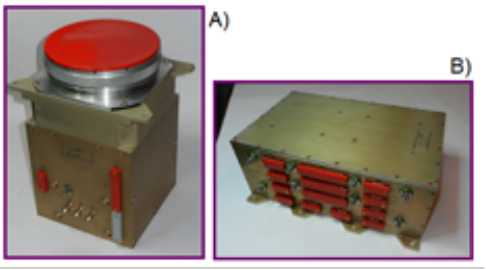

Figure 1: Photo of the BDRG instrument. A) Detector box. B) Data analysis box.

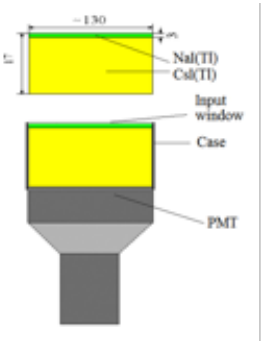

Figure 2: Design of the BDRG scintillation detector.

2 Design and characteristics of BDRG gamma-ray spectrometer.

The BDRG instrument consists of 3 similar detector boxes, connected to a data analysis box. The axes of BDRG detectors are shifted by 90 **HERE** with respect to each other. The detectors have a cosine-like angular dependence for the sensitive area (FWHM 60 **HERE**) that allows one to determine the coordinates of GRBs with an accuracy of several degrees for bright GRBs via a comparison of the detector readings. The sensitivity of the instrument is about 10^{-8} erg/cm^2.

Each detector consists of optically coupled thin (3 mm) NaI(Tl) and considerably thick (17 mm) CsI(Tl) crystals. The thickness of NaI(Tl) is opti-

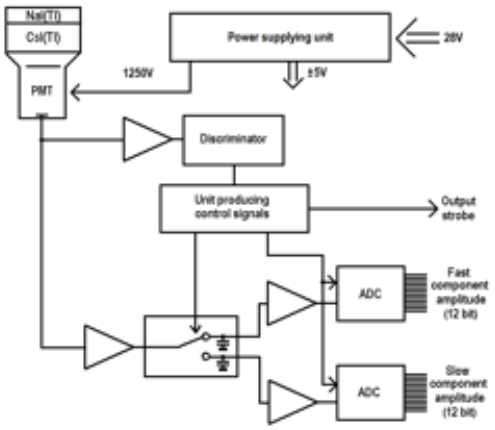

Figure 3: Functional diagram of the BDRG detector box electronics.

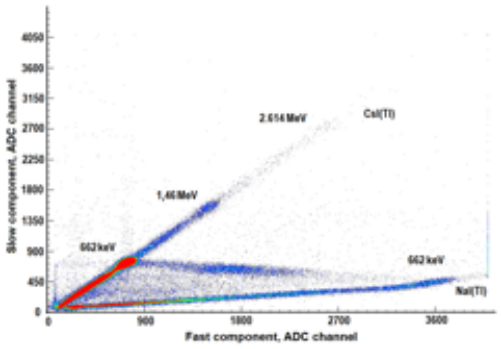

Figure 4: Example of 2D-diagram (slow part of PMT pulse vs fast one) for ^{137}Cs gamma-rays.

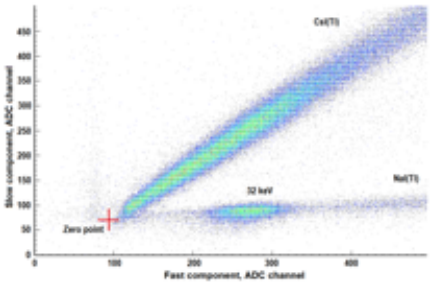

Figure 5: Example of 2D-diagram (slow part of PMT pulse vs fast one) for ^{137}Cs gamma-rays: low part of energy range.

mized for the soft part of the energy range. CsI(Tl) plays the role of active shield for soft radiation, while being the main detector for hard one. Working ranges are 0.01-0.5 MeV for the NaI(Tl) detector and 0.05-3 MeV for the CsI(Tl) one. Each detector box has a mass $\sim$ 5.5 kg and power consumption $<$ 3W. The power consumption of the data analysis box is $\sim$ 15 W.

2.1 Detector box electronics design

The functional diagram of the BDRG detector box electronics is presented in Fig. 3.

A pulse of current arrives from the PMT to the amplitude discriminator generating an event start pulse. This pulse starts the signal control sequence. One of the control signals is used to the change the SPDT state so that two parts of the primary PMT output pulse are integrated independently. The first one is proportional to the amount of light collected during the first 800 ns of the pulse (the so called Fast component) and the second one is proportional to the amount of light collected during the next 2 μs (the so called Slow component).

Both signals are digitized by correspondent successive approximation ADCs. When the conversion is finalized, parallel codes of the fast and slow components arrive to the BDRG information box (BA BDRG) together with a request of "output strobe". The BA BDRG runs the algorithm of event processing in order to determine in which scintillator the interaction took place and the value of the energy release. Then, a sequence of data frames of several types is formed in the BA BDRG box and the analysis of the data for GRB trigger condition is provided.

2.2 Detector box calibration

The measurement of the energy release in a detected event must be done separately for NaI(Tl) and CsI(Tl) events. The correspondent procedure used for the BDRG instrument can be explained using a 2D-diagram where the x and y values for each event are its fast and slow component amplitudes. An example of such a diagram for a ^{137}Cs gamma-source is presented at Fig. 4.

One can see two straight lines for NaI(Tl) and CsI(Tl) events. Points between these lines correspond to the events for which a Compton interaction of a gamma-quantum took place so that the energy was released in both crystals. The spots of events with energy release 662 keV corresponding to the total energy absorption peak the of ^{137}Cs source radiation as well as 1.46 MeV and 2.614 MeV events from background isotopes ^{40}K and ^{208}Tl (from the ^{232}Th decay sequence) are seen.

The low energy part of ^{137}Cs 2D-diagram is presented in Fig. 5. One can see a spot of 32 keV X-rays from the radioactive source. These events are present only in the NaI(Tl) part of detector because most of such X-rays interact with it and do not reach the CsI(Tl) layer. The red cross shows a zero point corresponding to zero amplitude of the PMT pulse. This point is shifted from (0,0) by some constant small voltage offset at the ADC

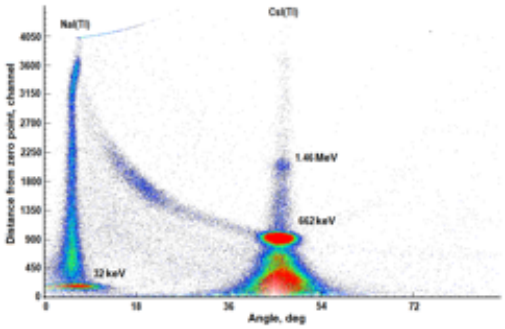

Figure 6: 2D-diagram of ^{137}Cs gamma-rays transformed to polar coordinates (dependence of distance from zero point on angle).

input. The energy can be determined from the distance between the point of the event and this zero point. The coefficients in the corresponding linear formula are different for different scintillators and must be determined individually from calibration measurements.

The 2D-diagram can be transformed to the polar form, given the angular dependence of the distance between the event point and the zero point. An example of such a diagram is presented in Fig. 6. The y-coordinate is now responsible for energy and the x-coordinate allows one to determine the kind of scintillator crystal. One can see that the events in NaI(Tl) and CsI(Tl) are well separated for an energy release greater than 10 keV.

Calibration of BDRG detectors was done by using a number of radioactive isotopes listed in Tab. 1. Two background gamma lines were also used for calibration of the CsI(Tl) part of the detector in the high-energy range.

Individual calibrations were made for the NaI(Tl) and CsI(Tl) parts of each BDRG detector box as well as for main and redundant high voltage suppliers, since the redundant system provides a lower voltage for reliability. Sets of calibration lines (presented in Fig. 7) demonstrate the good linearity of all detectors. The energy resolution at 662 keV from ^{137}Cs is about 13% for both main and redundant systems. The main factor limiting the energy resolution is the non-uniformity of the PMT photocathode sensitivity.

Isotope	Energy	Isotope	Energy
^{241}Am	26.34	^{60}Co	1173
	59.54		1333
^{181}Hf	57	^{207}Bi	74
	133		569.7
	345.9		1063.7
	482.2		1770
^{137}Cs	32	^{40}K (background)	1460
	661.7	^{208}Tl (background)	2614

Table 1: List of gamma-sources used for BDRG calibration (energy values are in keV).

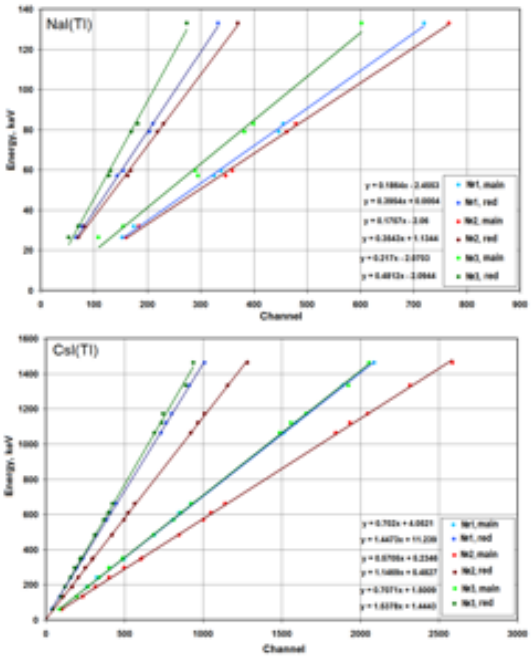

Figure 7: Calibration diagrams for 3 detectors of BDRG separately for main and redundant PMT power suppliers.

3 Production of the BDRG trigger

If BDRG monitoring readings show a fast increase of gamma-ray flux, the trigger signal if produced. Necessary conditions for trigger production are:

- Presence of fast rise of hard X-rays readings (channel 25-100 keV will be used in BDRG).
- Not too high rate in hard X-rays.
- GRB/imitation by electrons criterion based on NaI(Tl)/CsI(Tl) ratio (see below).

3.1 Search for fast rise of gamma-ray readings

The algorithm for search of gamma-ray reading fast rise is illustrated in Fig. 8.

History of detector readings is stored in a mem-

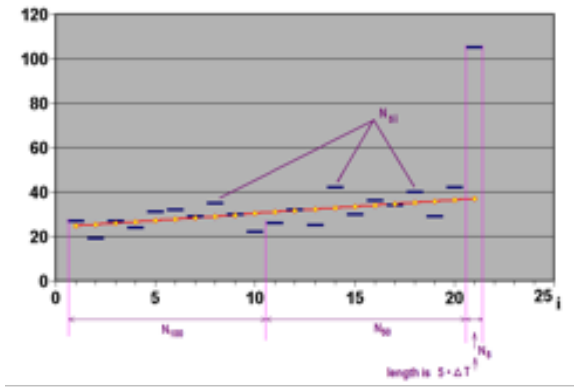

Figure 8: Illustration of the algorithm of search for fast rise of gamma-ray readings.

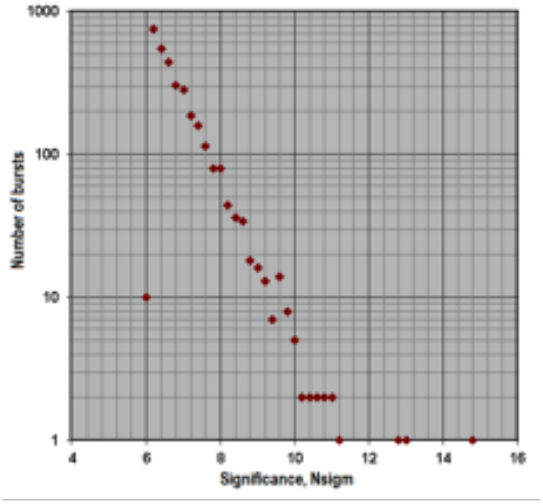

Figure 9: Illustration for the algorithm of search for fast rise of gamma-ray reading.

ory with temporal resolution ΔT (temporal resolution of burst data to be transmitted to Earth) for a time interval: $100 * \Delta$T. All history is divided in $5 * \Delta$T bins (row N_{5i}). The sum of N_{100} and N_{50} numbers of events for the first and the second half of history - are calculated (see Fig. 8). By means of linear regression the expected value for the next $5 * \Delta$T interval is calculated (named N_{5exp}). If $N_{50} < 30$, the mean value is used. The standard deviation σ is calculated for the difference between measured row N_{5i} and the regression one. Then, the values N_5 and N_{5exp} are compared. Burst trigger is set if:

$$\begin{aligned} N_5 &> N_{5exp} + N\sigma \\ N_5 &> 2. \end{aligned} \quad (1)$$

Here the value N is a number of standard deviations when the increase of the BDRG readings is considered significant.

Several time scales will be used for independent triggering:

1. 20 ms interval, 1 ms resolution of monitoring data;
2. 1 s interval, 50 ms resolution of monitoring data;
3. 20 s interval, burst data in event mode added.

3.2 GRB or its imitation by electrons criterion

It is essential to be able to discriminate between the fast rise of the BDRG readings caused by gamma-rays coming from a GRB and the bremsstrahlung X-rays produced by the satellite material when it passes some beam of electrons. The criterion used in the BDRG is based on the comparison between monitoring readings of NaI(Tl) and CsI(Tl) in different energy channels. If a GRB occurs, radiation comes to the NaI(Tl) side of the detector. Most of the secondary radiation from electrons comes from the satellite. The parameters of the criterion such as energy limit intervals and the NaI(Tl)/CsI(Tl) ratio threshold were chosen by modeling with Geant software. They can be changed by commands during the space experiment.

3.3 Choice of threshold value in GRB criterion

The threshold number of sigma (value N in Eq. 1) can be chosen by analyzing the empiric distribution of triggers on their significance. Fig. 9 shows an example of such a distribution for 20 ms triggering collected during 65 hours. The criterion for onboard triggering can be soft, allowing one to have $\sim$ 20 false bursts per day transferred to Earth so to avoid loosing any real GRB with enough amplitude. For the presented case $N_{sigm} > 9$. The criterion for the world net must be harder. The proposed value is $N_{sigm} > 12$ or even greater.

3.4 3.4 Estimation of GRB coordinates

GRB coordinates can be estimated by comparing the readings of the 3 BDRG detectors having a cosine beam of view. Their axes are shifted by 90° with respect to each other, therefore the GRB direction can be calculated from the formula:

$$cos\theta_i = \frac{N_i}{\sqrt{N_{12} + N_{22} + N_{32}}} \quad (2)$$

where θ_i is the angle between the detector axis and the burst direction and N_i is the number of events in the detector number i.

The accuracy of GRB localization depends on factors such as GRB brightness, hardness, and back-

fluence	kT, keV	Background rate, Hz					
		0	10	50	100	500	1000
1.0E-07	5	18.5	27	36	40	48	52
1.0E-07	10	8.4	10.3	16.5	21	33	38
1.0E-07	25	5.2	6	9.5	12	21	27
1.0E-07	50	5	5.6	9	11	19.2	25
1.0E-07	100	5.5	7	11	14	24	28
1.0E-07	300	8.5	11.5	19	24	37	43
1.0E-06	5	8	8.5	10.5	13	21	26
1.0E-06	10	4.5	4.5	5	5.5	8	10
1.0E-06	25	2.2	2.2	2.5	2.8	4.5	5.2
1.0E-06	50	2	2	2.4	2.7	4.5	5.2
1.0E-06	100	2.4	2.5	2.8	3.4	5.2	6.3
1.0E-06	300	3.7	4.1	4.5	5.2	8.3	10.5
1.0E-05	5	7	7	7	7	7	8
1.0E-05	10	4.5	4.5	4.5	4.5	4.5	4.5
1.0E-05	25	1.8	1.8	1.8	1.8	1.8	1.8
1.0E-05	50	1.6	1.6	1.6	1.6	1.6	1.8
1.0E-05	100	2.2	2.2	2.2	2.2	2.4	2.4
1.0E-05	300	3	3	3	3	3	3.5

Figure 10: Accuracy of GRB localization (in degrees).

ground level. The results of our modeling are presented in Fig. 10.

4 Structure and amount of BDRG data

Information from the BDRG will contain data frames of 3 main types: monitoring (count rate in 8 energy channels for NaI(Tl) and CsI(Tl)), Spectrum (724 channel spectra for NaI(Tl) and CsI(Tl)), and Event mode (primary values of fast and slow components for a fixed number of events combined with time data). Structure and amount of data are presented in Tab. 2:

Type of frame	**Time interval between frames**	**Daily amount, Mb**
Continuous (35 Mb per day)		
Monitoring	1 s	9
Spectrum	60 s	12
Event mode	60 s	14
Burst mode for fast/slow burst (2 Mb per burst)		
Monitoring	1-10 / 10-100 ms	1.4
Spectrum	5-10 / 20 s	0.3
Event mode	not regular	0.3

Table 2: Structure and amount of BDRG output data.

5 Conclusions

A number of tests on calibration and trigger production confirmed that BDRG is ready for the space experiment.

Acknowledgments

The work was performed with partial support by the Mega-grant number 11.634.31.0076

Science and Instruments for New GRB Missions

B. Grossan
Extreme Universe Laboratory, Moscow, Russian Federation & UC Berkeley, Berkeley, USA

Abstract

I present science motivations for new GRB measurement systems, then give a review of new instruments and detection capabilities that might be applied to these problems. I also discuss my own work on new missions. The talk includes a discussion of low-energy X-ray detection capabilites, instruments for sub-minute rapid optical response, polarization-sensitive X- and gamma-ray measurements, high-energy X- and soft gamma-ray instrumentation, and a discussion of new semiconductor detectors.

1 Introduction

1.1 Motivation

We are in an era where Swift could soon fail from old age or lack of renewed funding, where there are few planned missions, and where resources are modest. What can we do for cosmic gamma-ray burst (GRB) science in this era? In this talk I concentrate on instruments which can result in good localizations ($\sim$ few arc min) for follow-up studies, and I ignore most other capabilities.

1.2 What we know and don't know about GRBs

What we know:

We have hard data to support, or a fair amount of observations on:

- X, gamma light curves of LGRB ($\sim 10^2$).
- GRB extend well into EOR (z > 6).
- LGRB $\Leftrightarrow$ star-forming regions $\Leftrightarrow$ massive star SNe.
- NOT obviously standard candles.
- The GRB afterflow is likely related to prompt emission in a well-defined correlation [1].

. . . and much more.

What we don't know about GRB:

- z-distribution beyond $\sim$ a few (and few observations using GRB as tools for high-z universe study, such as measurements of HI and dust).
- Detailed prompt emission mechanism.
- Relation of prompt optical and gamma.
- Origin of Short GRB (SGRB).

Of course there is much more we don't know , such as the origin of light curve pulsations and other features (perhaps from an interrupted jet?), gravitational wave (GW) properties (of SGRB), etc. The point is that the rest of this talk I will discuss how new instruments will help us make progress understanding these items.

2 Exciting topics with potential for progress

2.1 High-z GRBs

High-z GRB are a hot topic. The Janus study [2] suggested that High-z GRBs are expected to be rare, and faint, so you need a wide field instrument for high event rate. Also, the study and instrument design emphasized low-energy response. Since the peak energy in $\nu \cdot F_\nu$ is typically 160 keV [3] for observed GRB, they assumed that E_{peak} of high-z GRB would be ~ 160 keV$\cdot(1+z_{typ})/(1+z)$, where z_{typ} is the typical redshift of currently measured GRB, $\sim$ 1.5. They therefore put forth a design maximizing low-energy sensitivity.

The biggest uncertainty with the Burrows et al. study is that there is no evidence for the scenario it assumes. Most high-z GRB do not have good measurements of E_{peak}; however, it is a well-known result that there is no good correlation between red shift (or any obvious function of red shift or distance) and E_{peak} in actual observations, nor a fluence or peak flux trend that may be predicted by distance (e.g. [4]). Despite the obvious, attractive, and simple theoretical idea that instruments with lower energy sensitivity must be better at detecting proposed high-z populations of GRB, there is no defending this idea in the face of now exten-

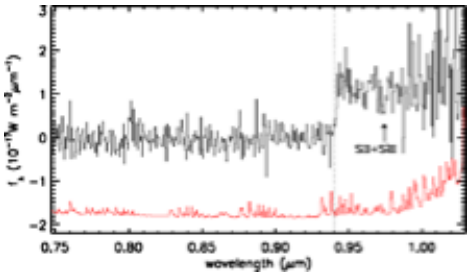

Figure 1: Spectrum of GRB080913 taken from [5], z = 6.7. The red line gives one sigma error, the black line is the spectrum.

sive data over a wide range of z. It is likely that detection/instrument bias and evolution properties make this more complex than simple distance and red shift arguments can explain. Finally, there have been no low-energy sensitive wide-field GRB instruments to test this hypothesis since HETE. HETE was certainly not dominated by z > 6 bursts, but it may be argued that it was not sensitive enough and did not operate long enough to detect such bursts.

Most authors agree that the epoch of reionization (EOR) ends by z ∼ 6; GRB spectra for z > 6 have already been measured (Fig. 1; [5]), so there is no doubt that GRB can act as the light source we need to shine through the universe so we can probe this far-off region. Hubble ultra deep field galaxies are far too faint for spectroscopy, but not GRB! (z=6.7 GRB in Figure 1 shows the Lyman alpha absorption very clearly, and SiII is also visible.) If we could find a large enough number of high-z GRB, and we could be on them with spectrographs early enough, while they were still bright, we could build up a picture of the IGM in the early universe. Each high-z GRB would be a "pencil beam" probe of the EOR (Fig. 3, [6]).

2.2 GRB emission mechanism

The ultimate physical process of GRB emission in standard theories is nearly always synchrotron emission. Because of the symmetry axis of the magnetic field, prompt GRB emission is therefore expected to be polarized. Can we verify this? Are GRBs Polarized? Answer: Yes, or anyway, at least one has been measured with a good consensus that the measurement is robust, with statistics well under control [7] with IKAROS GAP. Other cases have been not so clear. The area of X-ray/gamma-ray polarization observations of GRB is still wide open, despite the fundamental nature of this topic.

X-ray/gamma-ray polarization information usually comes from a Compton-telescope type instrument. However, several new generation solid-state detectors have some polarization sensitivity (e.g. NuStar). (Note that Tanimori, in his talk in this conference, discusses his electron tracking instrument that fully reconstructs the event including the direction and energy of the electron.)

Optical polarimetry measurements to date are almost always during the afterglow phase, not commencing early enough to cover prompt emission. The measurements of the polarization of the afterglow vary. Without a clearly separate measurement of the prompt emission component, not much is learned about the prompt emission process. This is the same old rapid-response problem: getting on a GRB very early allows measurement of the prompt emission and likely means measurement when the burst is bright and easy to measure. However, moving a big telescope quickly, and dealing with clouds and daylight is a very tough challenge for ground-based instruments.

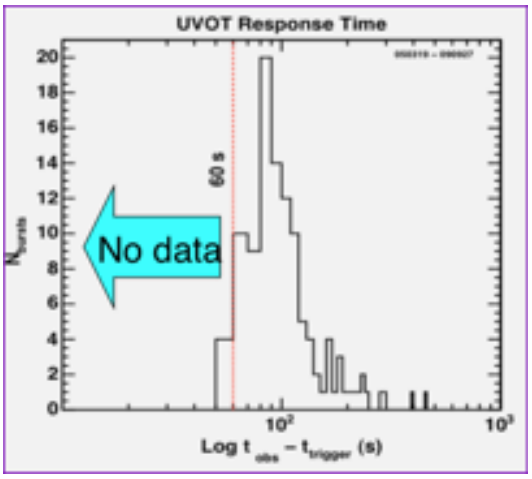

Figure 2: Histogram of Swift optical response time.

2.3 What is the relation between prompt optical and gamma-ray emission?

We are data starved on prompt optical emission. Swift optical response is strictly limited: few data t < 60 s have ever been recorded; the figure suggests that the cause is a limit to technical abilities of the spacecraft (e.g. the settling time), so this will not improve with more observations. ROTSE-III and other ground-based automated response telescope are important, but in the end produce only a small number of bursts with $t_{rise} < 60$ s.

If we could observe GRB optically with very fast response, there are many exciting things we could do. There is one, unique GRB with high-quality data in more than seven years of Swift operation, the "naked eye" burst 080319b [8].

This one example shows us that many things are possible with prompt optical data. Given the simple assumptions in [9] , we can measure an independent optical bulk Lorentz (BLF) factor from the time of the optical peak. Sari & Piran [10] predicted that an early and bright optical peak (or not) would tell if the jet were magnetic or baryon dominated. (The figure shows two peaks; what does that mean?) These data are good enough to look for cross-correlations and delays. Give us 100 of these, and imagine what we could learn! Unfortunately, we have only one after seven years of Swift.

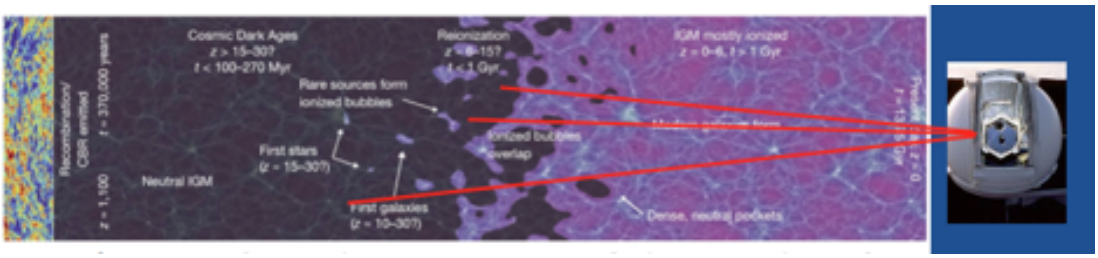

Figure 3: Cartoon with artwork taken from [6]. Each high-z GRB spectrum would be a "pencil beam" probe of the early universe IGM, which leaves its imprint in the spectrum.

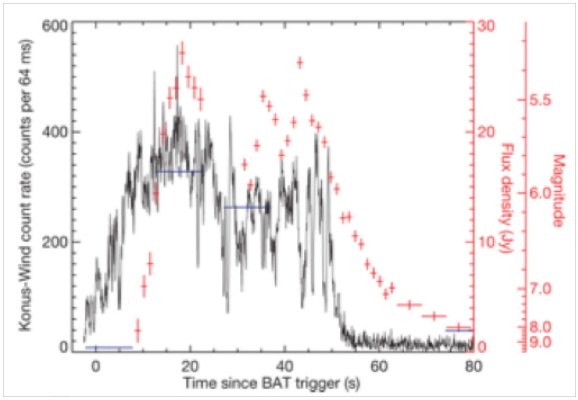

Figure 4: "Naked Eye Burst" X-ray (black) and TORTORA optical (red) and ROTSE-II (Blue) light curves [8].

2.4 Dynamic dust evaporation via Color measurements

When a GRB explodes, it has more than enough hard photons to vaporize circumstellar dust. The models for this, [11, 12, 13], suggest that the time scale for this process is $\sim$ 60 s. The implications of this are clear: in the early phases of IR-optical emission (Fig. 5) the blue end of the spectrum is heavily absorbed, whereas the IR part of the emission is much less absorbed. By looking at IR-optical colors, we can watch this process dynamically, learning about the amount and composition of the circumstellar dust. This is extraordinary - What other way is there of studying dust around a single star in another galaxy, to say nothing of studying it at z $\sim$ 1 to 2 (depending on how red your instruments respond)? Most ways of studying dust do not distinguish between the dust local to the star, that of the stellar group, and that associated with larger structures such as arms.

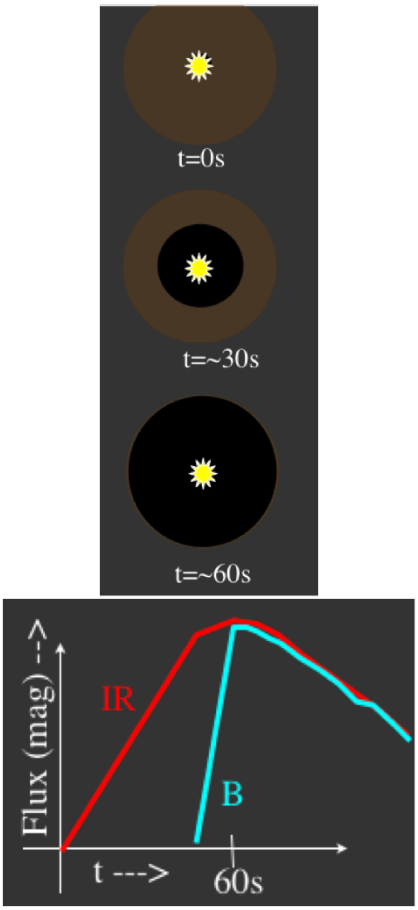

Figure 5: Dust Evaporation The cartoon above shows the GRB (star shape) initially surrounded by dust (brown), which evaporates as time progresses to give smaller dust column and reduced reddening.

2.5 Short GRB

We have as of this writing $\sim$18 to 25 [14] optical detections of Short-type GRB (SGRB), compared to hundreds for Long-type (LGRB). There are simply no detailed optical light curves like the naked eye burst for SGRBs; these are too faint for

small, fast telescopes on the ground. There are few well-sampled optical-IR light curves covering multiple bands, and fewer still spectra. With lower red shifts than LGRB, SGRB often have large offsets from their hosts, lower fluence, and different (smaller) spectral lags. If you could just build an instrument that would give you 100 well sampled, multi-band SGRB light curves, it would be a game changer for this type of GRB. It would be like going from Beppo-Sax to Swift. The importance of learning more about SGRB cannot be overstated, because these will likely be the bread-and-butter of the first generation of gravitational wave (GW) astronomy. Without an instrument capable of identifying these events (GW location is terrible, a large fraction of the sky) operating when the GW observatories come on line, such observatories could be of little value, as their events would be without EM confirmation or location.

3 New instrument capabilities

How do we build new instruments to address all the science topics I mentioned above? In my presentation at the conference I showed an image with IKAROS cut-and-pasted onto one side of Swift, and FERMI stuck on the other, to facetiously point out the difficulty of combining many different capabilities in a single, realistic observatory.

3.1 Low-E response?

As discussed in Sec. 2.1, there is little data to support low energy detection capability as the critical path to finding more high-z GRB. However, low-energy capability does make your instrument more sensitive, and it does add new information.

Swift BAT CZT detectors respond $\sim$ 15-150 keV. They have no lower energy response because *very* low noise electronics are required for $<$ 10 keV response? with CZT or CdTe- this is still difficult today, a capability of only a few expert labs.

The wide-field instrument on SVOM has CdTe detectors, for $\sim$ 5-10 keV minimum energy threshold. (I note that this mission has been downsized or delayed the last time I heard about it). In [2], the detector chosen for JANUS for low-energy response was Si H2RG detectors, sensitive down to 0.5 keV, but up to only 20 keV. This mission was not selected for a start, so for now there are no high GRB rate instruments with this capability. I defer further discussion of this capability to the end of this talk.

I do want to mention that there is another way of approaching the high z GRB problem. In the talk by Iyudin in this conference, he will discuss detection of GRBs with GROME [15, 3]. If there are high columns surrounding the high-z GRB, such an instrument could detect a GRB, and without optical follow-up, measure the redshift via nuclear resonant scattering. See the proceedings version of this talk for further details.

3.2 "Prompter" optical

Many people at this conference are familiar with the Ultra-Fast Flash Observatory (UFFO) Pathfinder [16]. This GRB mission is an international collaboration led by Il Park and his Group (currently at Sungkyunkwan University, Seoul), and including many scientists at MSU/SINP and our Extreme Universe Lab. The UFFO will have a wide-field X-ray coded mask camera, the UBAT (UFFO Burst Alert Telescope), and an optical-UV telescope, the SMT. The system boasts optical response beginning within a fraction of a second of trigger. The SMT is pointed via a beam-steering mirror. While Swift points the entire spacecraft, taking no less than 60 s until pointing and settling is complete, this system moves only a beam-steering mirror to point the telescope, a much faster system.

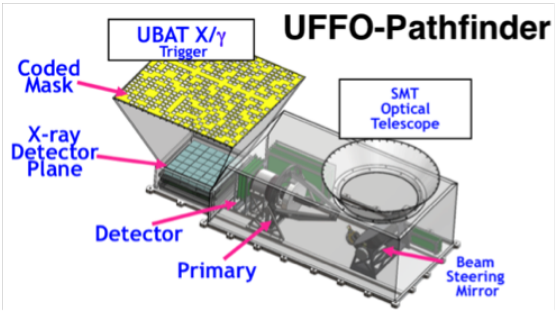

Figure 6: Schematic of UFFO-Pathfinder. The two main instruments are the UBAT X-ray coded mask camera, for burst detection and coarse localization, and the SMT telescope and optical camera for early measurement of optical emission. The mirror can point and settle in less than one second.

This is a small pathfinder instrument, with a total of $\sim$ 20 kg, 12W, and 190 cm^2 of detecting area. The aperture of the optical telescope is 10 cm. This is intended as a proof-of-concept mission, and we expect it to be launched some time in 2013 on board the Lomonosov spacecraft (also a collaborative project with most instruments and spacecraft platform infrastructure centered here at MSU/SINP).

What set of capabilities could we put on a Next Generation Rapid Optical Response mission to fully exploit this new time domain? My collaborators and I proposed instruments for a NASA mission of opportunity. This proposal was not accepted, but we continue to work on this with our partners from MSU SINP/EUL. The MSU SINP/EUL expertise in high-energy space instruments is critical to our

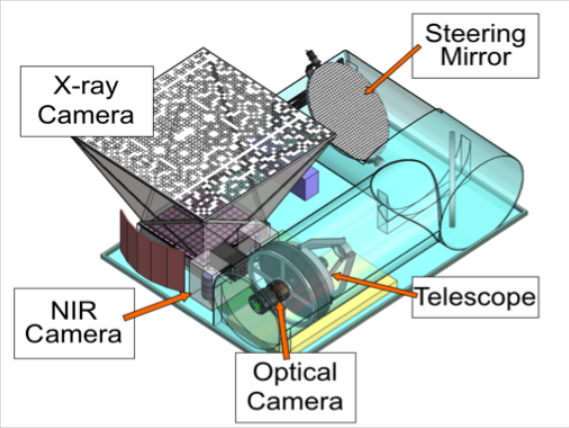

Figure 7: Rendering of the UFFO-100 (compact configuration) design (I. Park and UFFO Collaboration, re-labeled). In this configuration, the overall cube-shaped envelope is minimized by use of a folding mirror (which may not be appropriate for IR use). Figure by Soomin Jeong/UFFO Collaboration.

project. Disclaimer: I discuss here only my own ideas as to the choice of instruments and other details which may not be approved by any collaboration. A rendering of a very compact, approximately cubic envelope version of a Next Generation Instrument (by Soomin Jeong of the Park Lab) appears in Figure 7.

Prof. Panasyuk of MSU/SINP has been in informal discussions regarding possibilities for launching such an instrument. Among the possibilities discussed have been on a Resurs-P and on the International Space Station. The mission definition here is for a low-earth orbit, $\sim$ 120 kg, $\sim$ 150 W payload.

By scaling our instruments up from the UFFO pathfinder, we find that we can produce a wide-field X-ray shadow mask camera with 1000 cm^2 collecting area, a beam-steered optical telescope of 30 cm aperture, and two cameras in this mass budget.

You will note that there is no analog to the Swift XRT in this concept. The XRT is a complex and large instrument. We can learn many new things about the "same old" Swift population of GRBs (which we would detect with such an instrument) if we have the add rapid-optical/IR response capability. We would get a high quality position for our optically detected bursts, fulfilling this part of XRT's function.

Besides scaling up the UFFO in size, the major addition for this next generation instrument is two cameras. A dichroic splits the beam from the optical/IR telescope into two bands, one for the Optcam - 0.38-0.6 m, and one for the R-Icam a HgCdTe array sensitive to 0.6-1.7 μm. The use of a dichroic allows the simultaneous measurement of the two bands, allowing us to dynamically monitor a broad-band slope. This can be used for the dynamic dust measurements discussed above. The NIR instrument allows us to see moderately extinguished bursts, boosting the event rate by $\sim$ 50% above that of the Swift UVOT. More details of this design are discussed in [17].

3.3 X/gamma polarization measurements

Compton telescopes, described elsewhere (e.g. [18]) are typically used for detection in the 200 keV to MeV energy range. In addition to providing high-energy detection, they can provide polarization information via reconstructing the Compton scatter interaction, which is polarization dependent. The SGD instrument on Astro-H, a hybrid Si and CdTe instrument is an example of a modern Compton camera design [19]. I want to note that the GROME/GRIPS instrument, discussed in other talks [15, 3], provides this capability, and a talk by Tanimori describes his Electron Tracking Compton Camera, which also follows the recoil electron for even better reconstruction of Compton events.

3.4 High Energy response

Instruments with higher energy response get more SGRB, as SGRB have a very hard spectrum compared to either the X-ray background or LGRB (see Fig. 9). $E_{peak,LGRB} \sim 160$ keV; $E_{peak,SGRB} \sim 490$ keV [3]. BATSE and Fermi get $\sim$ 24% and 18% SGRB respectively [20], compared to Swift's $\sim$ 10% [21].

For typical SGRB spectral slope, pretending for simplicity that the diffuse X-ray background is the only background (it isn't, instrument background is important), integration to an upper energy limit of many hundreds of keV still increases S/N; for LGRB, above 200 keV there is little increase in S/N (Fig. 9).

As higher energy instruments measure more SGRB and provide a means to measure and study the peak energy (which Swift often misses), why aren't more flown? To quote from the Von Ballmoos talk during this conference, about $>$ 100 keV instruments and related issues: Terrible, Unlucky, Very DIfficult, Crazy. The critical part of this is his plot of the background in a modern Ge detector: the background increases $\sim$ 1000 times between 25-50 keV, then continues as a broad bump to around 1/10 of the Crab, until dropping around 1 MeV (in cts/s/cm^2/MeV).

Ideally, such an instrument would also provide optical follow-up location, typically requiring r $<$ 15 (typical optical FOV), and for a decent event rate $\geq$ 1.5 sr FOV , similar to Swift-BAT. To understand the challenge, consider a simple and direct approach with a coded-mask instrument like Inte-

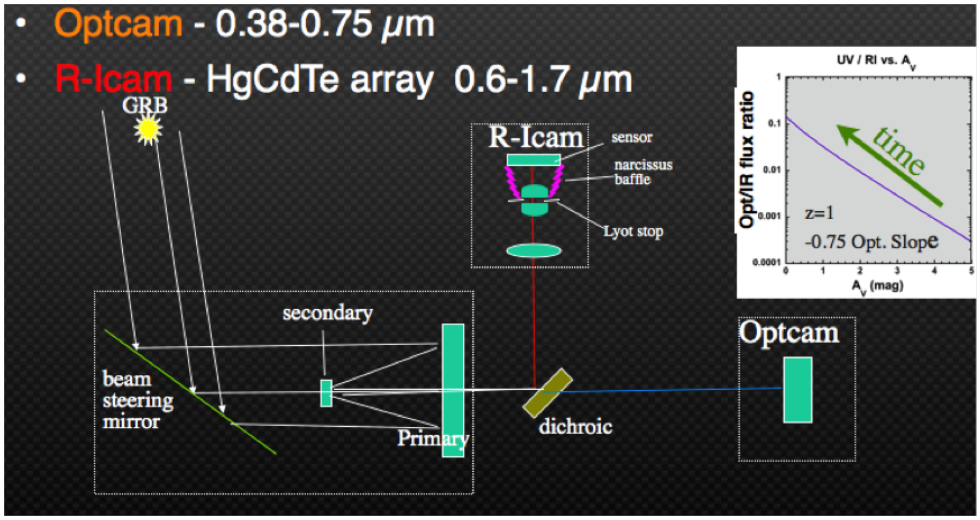

Figure 8: Schematic of the Optical Instrument, including an optical and IR camera to measure two simultaneous bands. Measuring the ration of the optical to IR flux, we can estimate the dust column to the GRB, and watch it change in time.

gral's ISGRI, with CdTe detector plane sensitive to $\sim$ 1 MeV and supplemental CsI detectors for sensitivity to 10 MeV. This kind of instrument is very heavy and complex, requiring an additional system of active veto detectors not on an instrument like BAT, but its 19 deg. FOV is much smaller than that of BAT, yielding a much lower GRB rate.

Such instruments continue to advance. Recently a clever innovation was made to increase collecting area in a coded mask instrument without actually making it bigger: make the mask tiles themselves active detecting area. For this purpose, in the HEMI instrument [22] from LBNL, by Amman and Vetter, they achieved a 1 cm^3 package including CZT detector and readout electronics that can be simply "plugged in" to a mask frame.

We might consider a tracking instrument plus a coded mask (see Von Ballmoos talk for examples). In this case, $\sim$ 10' positions have yet to be achieved. Ge is the likely detector type of choice; these have to be cryogenically cooled, again making for a heavy, complex, and possibly short-lived instrument. Reconstruction of events in a tracking detector can also be quite computationally intensive; this could be problematic for space, as space-approved processors are slow, which may impede rapid follow-up.

3.5 A new generation of semiconductor detectors

Since the SWIFT BAT detectors, there has been a revolution in new detector technology. A few years ago, the ECLAIRS wide-field coded mask instrument was proposed for what is now the SVOM mission. This team has achieved response $\sim$ 4 keV to 150 keV with the camera's CdTe detectors (and with CZT as well; Philippe Laurent; private comm.). For a photon flux log slope of -1.57 [21], typical for long GRB, this reduction in low energy threshold yields more than a factor of 2.7 increase in the number of source photons. There are two requirements to achieve this: First, the detectors must be cooled to -20° C, requiring power and mass for the cooling system. Second, very low-noise electronics must be used, requiring very specialized experience in the design and fabrication of such systems. The increase in the photon flux is a substantial reward for the additional effort, however.

The Proposed JANUS mission proposed uses Hybrid CMOS Si detectors with 0.5-20 keV response, detectors and electronics both purchased from Teledyne [1]. HETE used Si CCDs optimized for X-rays; these are typically integrating detectors with poor time resolution. The LOFT mission will use Si Drift detectors, optimum for the very large area.

A recent entry from particle physics is double-sided Si strip detectors DSSSD, which will be used on Astro-H. (See the excellent figures in [23]). One side of the device gives the X coordinate and the other gives the y coordinate of each event, simply by which strip collects the charge. These are widely produced: many groups have skills to make good readout electronics, and DSSDs are now produced commercially, even down to 25 μm spacing, rivaling good lab production. For many instruments, the cost of readout ASICs exceeds the cost of the detectors. Here, $N_{chan} \sim 2$ N not N^2, which could mean huge savings on electronics! The disadvantage is that the high energy response of CZT is missing. This can be recovered using multiple layers, however.

The NCT experiment (e.g. [24]) uses Ge double-sided strip detectors. With Ge, you get spectacu-

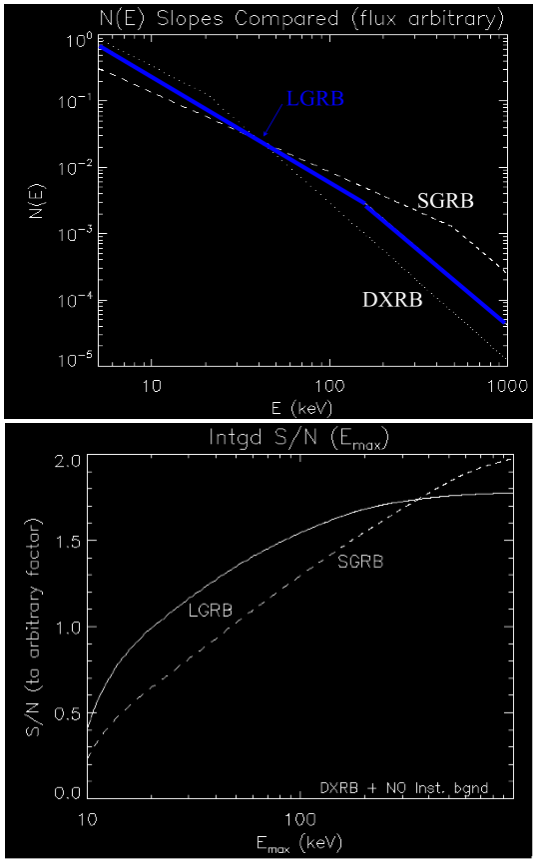

Figure 9: Top: Comparison of DXRB, LGRB, and SGRB slopes. SGRB are very hard. Bottom: Ignoring real instrument background, as you integrate SGRB to higher energies you still increase S/N with no turnover to hundreds of keV; LGRB turn over drastically past 200 keV.

lar spectral resolution (0.4% at 1 MeV). NCT also gets depth information for tracking. The drawbacks include the need for cryogenic cooling, heavy and power hungry, and location requires multiple iterations of maximum entropy calculations (possibly a problem for fast location) and not readily commercially available.

4 Summary

Many topics in GRB Science can be addressed directly by new instruments. Some of these are straightforward, some incorporating commercially available "out-of-the-box" detectors. Others require substantial optimization, specialized design, skills, and advanced development. Recent advances in solid state detectors give us many tools to advance GRB science; mostly we are limited only by our imagination (though budgets are also a challenging additional constraint).

Acknowledgments

I would like to acknowledge the staff of EUL for their expert help in putting on this conference, and the financial support of the Ministry of Education of the Russian Federation for their grant for our Extreme Universe Laboratory.

References

[1] Bernardini, M. G., et al. MNRAS **425**, 1199 (2012).

[2] Burrows, D., MSAIS **21**, 59 (2012).

[3] Greiner , J. et al., Exp.Astr. **23**, 91 (2009).

[4] Margutti, R., et al. MNRAS **accepted**, (arxiv1203.1059) (2012).

[5] Patel, M., et al., *Astronomy & Astrophysics* **512**, L3 (2010).

[6] Robertson, B. E., et al. Nature **468**, 55 (2010).

[7] Yonetoku, D., et al., *Astrophys. Journal* **757**, L1 (2012).

[8] Racusin, J. L., et al., Nature **455**, 184 (2008).

[9] Molinari, E. et al., *Astronomy & Astrophysics* **469**, 13 (2007).

[10] Sari, R., Piran, T., *Astrophys. Journal* **520**, 641 (1999).

[11] Perna, R., Lazzati, D., Fiore, F., *Astrophys. Journal* **585**, 775 (2003).

[12] Oates, S. et al., MNRAS **395**, 490 (2009).

[13] Perley, D. et al., MNRAS **406**, 2473 (2010).

[14] Berger, E., et al., , arXiv:1209.5423 (2012).

[15] Iyudin A.F., AIP C **1054**, 205 (2008).

[16] Park, I. H. et al., SPIE Proc. **8443**, 84430I-84430I-10 (2012).

[17] Grossan, B., et al. , 2012, SPIE Proc. **8443**, 84432R-84432R-13 (2012).

[18] Schoenfelder, V., et al., *Astrophys. Journal Supp.* **86**, 657 (1993).

[19] Tajima, H. et al., SPIE Proc. **7732**, 773216-773216-17 (2010).

[20] Paciesas, W. S., et al., *Astrophys. Journal Supp.* **199**, 18 (2012).

[21] Sakamoto, T. et al., *Astrophys. Journal Supp.* **195**, 2 (2011).

[22] Zoglauer, A., IEEE Conf. Pub. , 887 (2009).

[23] Takeda, s. et al., NIMPA **579**, 859 (2007).

[24] Boggs, S. E., SPIE Proc. **6266**, 626624 (2006).

Gamma-ray Bursts in the Fermi Era

Pawan Kumar
University of Texas, Austin, TX 78712

Abstract

After a brief overview of GRBs I will focus of recent developments in our understanding of gamma-ray burst prompt emission mechanisms. Properties of high energy emission (¿100 MeV) detected by Fermi from a number of bursts and their possible origin will be described, and the recent announcement by the ICECUBE collaboration regarding upper limit on neutrino flux from GRBs will be discussed. I will also report on recent measurements of magnetic fields in highly relativistic shocks associated with GRBs.

1 A brief overview of GRBs

The serendipitous discovery of Gamma-Ray Bursts (GRBs) in the late sixties by the Vela satellites puzzled astronomers for several decades: GRBs are pulses of gamma-ray radiation (typically lasting for a few seconds), with a non-thermal (broken power-law) spectrum peaking at 10300 keV, and can be seen a few times a day from random directions (eg. [1]–[3]). Their spectacular nature, the more recently established origin in the distant Universe, and their connection with supernovae explosions and black-hole/neutron-star formation, have placed the study of GRBs at the forefront of astrophysical research (eg. [4]–[8]). The launch of Compton Gamma-Ray Observatory (CGRO) in 1991 was the first major step toward a better understanding of the GRB phenomenon. The Burst and Transient Source Experiment (BATSE) onboard CGRO established the isotropic distribution of these explosions at a very high statistical significance and also showed the deviation of their brightness (defined by the burst peak flux) distribution from Euclidean at the faint end [3]. These were strong evidence that the bursts are at cosmological distances (eg. [9], [10]). The firm confirmation of the cosmological distance to GRBs was obtained in 1997, when the BeppoSAX satellite provided angular position of bursts to within 5 arc-minutes (more than a factor 10 improvement compared with the Compton Gamma-ray Observatory) which enabled optical and radio astronomers to search for counterparts for these explosions. A rapidly fading X-ray, optical and radio emission (the "afterglow") accompanying a GRB was found in February 1997, about a day after the detection of a burst, and led to the determination of burst redshift. It launched a new era in the study of GRBs which has led to wealth of new information and a much deeper understanding of these enigmatic explosions (eg. [11]–[13]). It was expected from theoretical considerations that GRB outflows are highly relativistic e.g. [14], [4]). We now have direct observational confirmation of this provided by the measurement of "superluminal" motion of the radio afterglow of a relatively nearby burst GRB 030329 [15].

The redshifts and burst fluences showed that GRBs radiate between 10^{51} and 10^{54} ergs, if isotropic. We now know from breaks in optical and x-ray afterglow lightcurves that GRBs are highly beamed and the true amount of energy release in these explosions is 10^{50}–10^{52}ergs [16]–[18].

Our understanding of GRBs has improved enormously in the last 15 years due to the observations made by several dedicated γ-ray/X-ray satellites (BeppoSAX, HETE-2, Integral, Swift, Fermi) and the follow-up observations carried out by ground-based optical and radio observatories. Much of this progress has been made possible by the monitoring and theoretical modeling of the long-lived afterglow emission following the burst.

The follow-up of GRBs at longer wavelengths (X-ray, optical, and radio) has established that the afterglow light-curve decays as a power-law with time ($F_\nu \propto t^{-1}$) and has a power-law continuum ($F_\nu \propto \nu^{-0.9}$). The forward-shock caused by the ejecta interaction with the ISM [19] provides a natural explanation for these observations. The synchrotron radiation in the forward shock provides very good fit to the mutiwavelength afterglow data for GRBs. In many cases, the decay of the optical or X-ray afterglow light-curve steepens to $F_\nu \propto t^{-2}$ a few days after the burst. The most natural explanation for this steepening (foreseen by Rhoads[20]) is that GRB outflows are not spherical but collimated into narrow jets. As the ejecta are decelerated and the strength of the relativistic beaming diminishes, the edge of the jetted ejecta becomes visible to the observer. The finite angular extent of the ejecta leads to a faster decay of the lightcurve (a so-called "jet-break").

The jet initial angular opening and kinetic energy can be obtained by modeling the broadband emission (radio to X-ray) of those GRB afterglows whose light-curve fall-offs exhibited a steepening. From these we found that the opening angle of GRB jets is anywhere from a few degrees to several tens of degrees, and this collimation reduces the required

energy budget by a factor 10–10^3 relative to the isotropic case; the true amount of energy release for most long duration GRB is found to be $\sim 10^{51}$erg ([16], [21], [18]).

The evidence for association of long-duration GRBs (those lasting for more than 2s) with core collapse SNa comes from two different kinds of observations: (i) GRBs are typically found to be in star forming regions of their host galaxies (e.g. [22]–[25]) (ii) for five GRBs SNa spectrum was detected: GRB 980425 [26], 021211 [27], 030329 ([28], [29]), 031203 [30], and 060218 [31]–[33]. Additionally, a subset of about 10 GRBs show at late-times (∼10 days) SNa-like bump" in the optical afterglows and simultaneously a change in color that is inconsistent with synchrotron emission [13]–[7].

The long standing question regarding the nature of short duration GRBs (those lasting for less than 2s) was resolved when a fraction of these bursts was shown to be associated with older stellar population, on average located at a lower redshift, and less energetic [34]–[37]. These observations are consistent with the old idea that these bursts originate from neutron star mergers ([38], [39]). However, there is no conclusive support for this model as yet.

The Swift satellite, launched in 2005, has led to a wealth of puzzling observations by filling the gap of about 7 hours in the early afterglow data that existed in the Beppo/SAX era and by providing continuous observations starting from about 50s from burst trigger [40]–[42]. Its X-Ray Telescope (XRT) discovered the existence of a sharp flux decay phase ($F_x \propto t^{-3}$) at the end of the prompt γ-ray emission that lasts for a few minutes, and is followed by a plateau lasting for about an hour during which the X-ray flux decreases much more slowly ($F_x \propto t^{-0.5}$) than expected in the standard forward-shock model. The former feature indicates that the GRBs and the afterglows are produced by two different mechanisms while the latter suggests that the forward shock that powers the afterglow is not fully developed at the end of the burst phase. These features likely reflect the behavior of the GRB central engine. If the central engine were to be an accreting blackhole then these features tell us about the accretion history which in turn can be used to determine some basic properties of the GRB progenitor star such as its radius and rotation speed [43].

Swift also discovered episodes of a sharp increase in the X-ray flux (flares) minutes to hours after the end of the gamma-ray burst ([44], [45]). The rapid rise time for the X-ray flux, with $\delta t/t \sim 0.1$, rules out the possibility that flares are produced as a result of inhomogeneities in the circumstellar medium where the curvature of the relativistic shock front limits $\delta t \sim R/2c\Gamma^2 \sim t$ or $\delta t/t \sim 1$ [46]–[48]. This suggests that the central engine in these explosions is active for a time period much longer than the burst duration.

GRB#	z	t (s)	flux erg/cm^2/s	E_{iso} (erg)
050904	6.3	225	3x10^{-8}	$\sim 10^{54}$
080913	6.7	8	7x10^{-8}	$\sim 10^{53}$
090423	8.2	10.2	6x10^{-8}	1.2x10^{53}
090429B	9.4	5.5	5x10^{-8}	3.5x10^{53}

Table 1: Bursts at redshift greater than 6; t is burst duration (T_{90}) in seconds.

1.1 Bursts at high redshifts

The highest redshift burst detected to date is at $z = 9.4$ which Swift discovered in 2009 (GRB 090429B). Table 1 lists the top 4 most distant bursts detected to date and their duration, average flux, and isotropic-equivalent energy release in γ-rays. The rest frame duration of 3 of these 4 bursts is less than 2s which be due to the fact that 150 keV photons detected by Swift/BAT have energy larger than 1 MeV in burst rest-frame, and GRB prompt lightcurves are known to be narrower in higher energy bands.

The luminosity, or energy release, for the high-z bursts in Table 1 is not exceptionally high. Considering that the sensitivity of Swift/BAT instrument for γ-ray transient events is $\sim 1.2 \times 10^{-8}$erg cm^{-2} s^{-1}, bursts like these can be detected by Swift up to a redshift of about 15. Because of their intrinsically simple spectrum, and extremely high luminosity, GRBs are expected to offer a unique probe of the end of cosmic dark age when the first stars and galaxies were forming.

2 High energy photons from GRBs

The Fermi Satellite has opened a new and sensitive window in the study of GRBs (gamma-ray bursts); for a general review of GRBs please see [49]–[6]. So far, in about three years of operation, Fermi has detected 30 GRBs with photons with energies >100MeV. The $>10^2$ MeV emission of most bursts detected by the LAT (Large Area Telescope: energy coverage 20 MeV to >300 GeV) instrument aboard the Fermi satellite shows two very interesting features [52]: (1) The first >100 MeV photon arrives later than the first lower energy photon ($\lesssim 1$ MeV) detected by GBM (Gamma-ray Burst Monitor), (2) The >100 MeV emission lasts for much longer time compared to the burst duration in the sub-MeV band (the light curve in sub-MeV band declines very rapidly).

There are many possible >100 MeV photons generation mechanisms proposed in the context of GRBs; see [53]–[54] for detailed reviews.

Shortly after the observations of GRB 080916C

[52], we proposed a simple idea that the >100 MeV photons from GRBs are produced via synchrotron emission in the external forward shock [55]. This proposal naturally explains the observed delay in the >100 MeV photons – it corresponds to the deceleration time-scale of the relativistic ejecta – and also the long lasting >100 MeV emission, which corresponds to the power-law decay nature of the external forward shock (ES) emission.

We note that the lower energy photons ($\lesssim$1MeV) have a different origin since the flux in the 50–300 keV band undergoes a steep decline ($t^{-3.3}$) at the end of the prompt GRB phase whereas the high energy photon flux declines much more slowly with time ($\sim t^{-1.2}$) that lasts for at least 1500s when the flux falls below the Fermi/LAT sensitivity (see Fig. 4 of [52]).

It is striking that the decay of the LAT lightcurve [$f_\nu(t) \propto t^{-1.2}$] is exactly what one expects for synchrotron radiation from the shock heated circumstellar medium (CSM) by the relativistic jet of a GRB. In fact, it is not only the time dependence of high-energy lightcurve from shocked CSM but also its magnitude that are the same as Fermi/LAT observations ([55] & [56]).

One can determine external shock parameters from early time ($t \sim 10^2$s) Fermi data and use that to **predict** late time optical and x-ray flux, which are found to be in excellent agreement with the observed data (Kumar & Barniol Duran, 2009 & 2010).

This exercise can also be carried out in the reverse direction, i.e. we can determine the external shock parameters from the late time (t $\gtrsim$ 0.5 day) x-ray, optical and radio data, and using these parameters calculate the flux at 100 MeV at early times ($t \lesssim 10^3$s). This "predicted flux" is also found to be in excellent agreement with the data obtained by Fermi/LAT. These results lend strong support to the suggestion that high energy photons from GRBs detected by Fermi/LAT, for $t \gtrsim 30$s, are produced via the synchrotron process in the external shock.

Following our initial analysis on GRB 080916C, a number of groups have provided evidence for the external forward shock origin of Fermi/LAT observations [57]–[60].

The external shock model for $> 10^2$MeV emission, however, faces a number of problems when confronted with the LAT data during the prompt GRB phase (the initial $\sim$ 30s following the GBM trigger). Foremost of these problems are the possibly short variability timescale for high-energy photons (about 1s) which is very difficult to produce in the external-shock (eg. [48]; but also [61]), correlation between $> 10^2$MeV and 10 keV–10MeV lightcurves, and a single Band function fit for the entire 10 keV—20 GeV data during the initial $\sim$ 30s for all GRBs detected by Fermi/LAT except 3 bursts [52]–[62]. These problems suggest that high-energy photons ($> 10^2$MeV) during the initial $\sim$ 30s are likely not produced in the external-shock.

3 Generation of magnetic fields in relativistic shocks

Magnetic fields are needed for synchrotron radiation in shocks. However, the process by which fields are generated is not well understood, nor is it clear by what factor does the ISM magnetic field need to be amplified in shocks in supernova remnants and GRBs.

The magnetic strength downstream of the shock front is expressed in terms of the energy fraction of the energy density of shocked plasma, ϵ_B, or

$$B^2 = 32\pi\epsilon_B n m_p c^2 \Gamma^2, \qquad (1)$$

where B is the magnetic field just downstream of the shock front, n is the density of the medium surrounding the GRB progenitor, m_p is the proton mass, c is the speed of light, and Γ is the Lorentz factor of the shocked fluid downstream of the shock front. If shock compression were to be the only mechanism amplifying the magnetic field downstream of the shock front, then B is given by $B = 4\Gamma B_0$, where B_0 is the seed magnetic field in the ISM field in the vicinity of the burst. For shock compressed magnetic field $\epsilon_B = B_0^2/(2\pi n m_p c2)$. Using a typical value for the ambient magnetic field of the Milky Way galaxy of $B_0 \sim 2\mu$G and a typical ISM density of $n = 1$ cm^{-3}, $\epsilon_B \sim 10^{-9}$ for the shock compressed field. The value for ϵ_B determined from GRB afterglow studies is, however, much larger of order 10^{-5}—10^{-1} (eg. [63]–[65]). The additional amplification, beyond the shock compression, could be due to the two-stream Weibel instability [66]–[67] and/or turbulence [68]–[72].

The excellent data provided by the Fermi/LAT for several bursts suggest that $\epsilon \sim 10^{-7}$ which could be a result of shock compression alone if the ISM field were to be about 20μG which is not unreasonable for star forming regions [56].

In an attempt to try to understand the large difference between earlier works on the determination of ϵ_B for GRB relativistic shocks mentioned above and more recent work on the Fermi bursts, Santana [73] undertook a systematic study of ϵ_B for a large sample of Swift GRBs. They employed several different techniques for determining ϵ_B so as to be able to cross-check results, and reduce uncertainties. We show in Figure 1 a histogram of their result for a sample of 35 GRBs and in Figure 2 the amplification factor above and beyond shock compression needed to account for the x-ray and optical

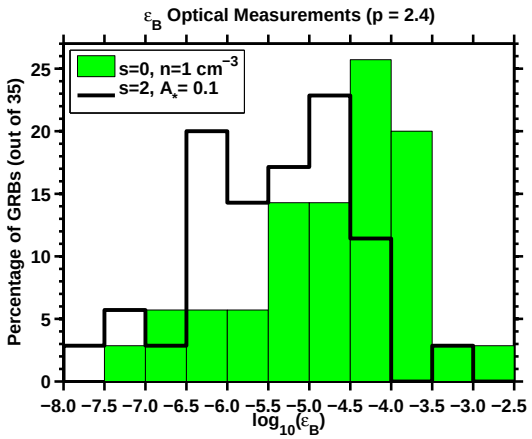

Figure 1: The filled-in histogram shows the ϵ_B measurements with electron distribution index, p, determined from the temporal decay of the lightcurve. The un-filled histogram shows the measurements of ϵ_B, assuming $p = 2.4$, for 35 bursts detected by the Swift satellite. For both histograms, a constant density medium with $n = 1$ cm^{-3} was assumed.

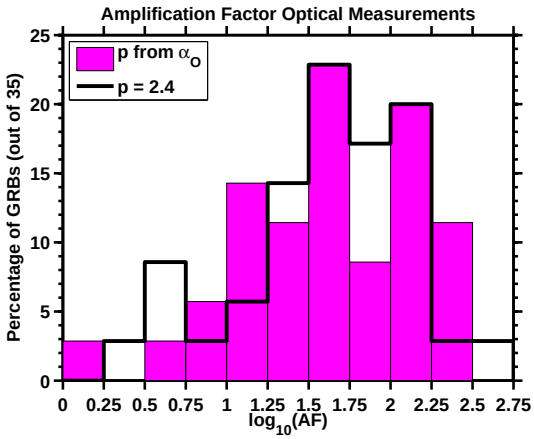

Figure 2: The filled-in histogram shows amplification factor for magnetic field in the shocked plasma when electron distribution index, p, is determined from the temporal decay of the lightcurve. The un-filled histogram shows the measurements of ϵ_B, assuming $p = 2.4$, for 35 bursts detected by the Swift satellite. For both histograms, a constant density medium with $n = 1$ cm^{-3} was assumed.

afterglow data for these bursts.

These figures show that shock compression alone is unlikely to be sufficient for most bursts, and that additional amplification by a factor of order ~ 20 is needed for synchrotron radiation in GRB relativistic shocks traveling into the circum-stellar medium.

Acknowledgments

I thank the organizers of this excellent workshop for the invitation to give a talk. This work has been funded in part by NSF grant ast-0909110.

References

[1] Band, D. et al 1993, ApJ, 413, 281.

[2] Kouveliotou, C. et al. 1993, ApJ 413, L101.

[3] Meegan, C. et al 1992, Nature 355, 143 .

[4] Piran, T. 1999, Physics Report 314, 575 .

[5] Meszaros, P. 2002, ARA&A 40, 137.

[6] Zhang, B. 2007, Chinese J. of Astronomy and Astrophysics, 7, 1.

[7] Woosley, S.E. & Bloom, J.S. 2006, Ann. Rev. A&A 44, 507.

[8] Fox, D.B. & Mészáros, P. 2006, New Journal of Physics 8, 199.

[9] Mao, S. & Paczyński, B. 1992, 389, L13 .

[10] Piran, T. 1992, ApJ 389, L45.

[11] Frail, D.A. et al. 1997, Nature 389, 261.

[12] Kulkarni, S.R. et al. 1998, Nature, 393, 35.

[13] Bloom J. S. et al., 1999, Nature, 401, 453.

[14] Fenimore, E. Madras, C. D. & Nayakshin, S. 1996, ApJ 473, 998.

[15] Taylor, G., Frail, D., Berger, E. & Kulkarni, S.R. 2004, ApJ, 609, L1.

[16] Frail, D.A. et al. 2001, ApJ 562, L55.

[17] Panaitescu, A. & Kumar, P. 2001, ApJ, 560, L49.

[18] Berger, E. et al. 2003, ApJ 590, 379.

[19] Mészáros, P. & Rees, M. 1997, ApJ, 476, 232.

[20] Rhoads, J. 1999, ApJ, 525, 737.

[21] Panaitescu, A. & Kumar, P. 2002, ApJ, 571, 779.

[22] Bloom, J.S., Kulkarni, S.R. & Djorgovski, S.G. 2002, AJ 123, 1111.

[23] Fruchter A. S. et al, 2006, Nature, 441, 463.

[24] Christensen L., Hjorth J. & Gorosabel J., 2004, A&A, 425, 913.

[25] Castro Cerón, J. M. et al., 2006, ApJ, 653, L85.

[26] Galama T. J. et al., 1998, Nature, 395, 670.

[27] Della Valle, M. et al. 2003, AA 406, L33.

[28] Hjorth, J. et al 2003, Nature, 423, 847.

[29] Stanek, K. et al 2003, ApJ, 591, L17.

[30] Malesani, D. et al 2004, ApJ, 609, L5.

[31] Modjaz, M. et al 2006, ApJ, 645, L21.

[32] Campana, S. et al. 2006, Nature 442, 1008.

[33] Pian, E. et al. 2006, Nature 442, 1011.

[34] Fox, D.B. et al. 2005, Nature 437, 845.

[35] Panaitescu, A. 2006, MNRAS, 367, L42.

[36] Bloom, J.S. et al 2006, ApJ, 638, 354.

[37] Nakar, E. 2007, Physics Reports, 442, 166.

[38] Eichler, D., Livio, M., Piran, T. & Schramm, D.N. 1989, Nature 340, 126.

[39] Narayan, R., Paczyński, B. & Piran, T. 1992, ApJ, 395, L83.

[40] Tagliaferri, G. et al 2005, Nature, 436, 985.

[41] Chincarini, G. et al 2005, astro-ph/0506453.

[42] Nousek, J. et al 2006, ApJ, 642, 389.

[43] Kumar, P., Narayan, R. & Johnson, J. 2008B, Science 321, 376.

[44] Burrows D. et al, 2005, Science 309, 1833.

[45] Chincarini G. et al., 2007, ApJ 671, 1903.

[46] Nakar, E. & Piran, T. 2002, ApJ 572, L139.

[47] Lazzati, D., & Perna, R. 2007, MNRAS 375, L46.

[48] Nakar, E. & Granot, J. 2007, MNRAS 380, 1744.

[49] Gehrels, N., Ramirez-Ruiz, E. & Fox, D.B. 2009, Ann Rev A & 47, 567.

[50] Meszaros, P. 2006, Reports on Progress in Physics 69, 2259.

[51] Piran, T., 2005, Reviews of Modern Physics, 76, 1143.

[52] Abdo A. et al., 2009, Science, 323, 1688.

[53] Gupta, N. & Zhang, B. 2007, MNRAS 380, 78.

[54] Fan, Y. & Piran, T. 2008, Frontiers of Physics in China 3, 306.

[55] Kumar P., Barniol Duran R., 2009, MNRAS 400, L75.

[56] Kumar P., Barniol Duran R., 2010, MNRAS 409, 226.

[57] Gao, W-H, Mao, J., Xu, D.; Fan, Y-Z, 2009, ApJ 706, L33.

[58] Ghirlanda, G., Nava, L., Ghisellini, G., Celotti, A., Firmani, C. 2009, AA 496, 585.

[59] Ghisellini, G., Nardini, M., Ghirlanda, G., Celotti, A. 2009, MNRAS 393, 253

[60] De Pasquale M. et al., 2010, ApJ, 709, 146.

[61] Dermer C.D., Chiang J., Mitman K.E., 2000, ApJ, 537, 785.

[62] Ackermann, M. et al. 2011, ApJ 729, 114.

[63] Wijers, R.A.M.J. & Galama, T.J. 1999, ApJ 523, 177

[64] Yost, S.A., Harrison, F.A., Sari, R., Frail, D.A. 2003, ApJ 597, 459.

[65] Panaitescu, A. 2005, MNRAS 362, 921.

[66] Weibel, E. S. 1959, Physical Review Letters, 2, 83.

[67] Medvedev, M. V. & Loeb, A. 1999, ApJ, 526, 697.

[68] Sironi, L. & Goodman, J. 2007, ApJ, 671, 1858.

[69] Goodman, J. & MacFadyen, A. 2008, Journal of Fluid Mechanics, 604, 325.

[70] Milosavljević, M. & Nakar, E. 2006, ApJ, 651, 979.

[71] Milosavljević, M., Nakar, E., & Zhang, F. 2007, ArXiv e-prints.

[72] Couch, S. M., Milosavljević, M., & Nakar, E. 2008, ApJ, 688, 462.

[73] Santana, R., Barniol Duran, R. & Kumar, P. 2012, submitted to MNRAS.

Past, present and future of hard X-ray and soft γ-ray measurements of GRB polarization

P. Laurent
APC, Univ Paris Diderot, CNRS/IN2P3, CEA/Irfu, Obs de Paris, Sorbonne Paris Cité, France

Abstract

Polarimetry is a new tool for understanding the Gamma-Ray Burst (GRB) mechanism, which begins to give important results. However, the data analysis for polarimetric studies is complex and should be undertaken with care. In this paper, we present the history of the GRB polarization measurements, highlighting the main results.

1 Compton polarimetry principles

Photons entering a typical Compton polarimeter [1], composed of several superposed spectro-imagers, are Compton scattered in a first detector plane, at a polar angle θ from their incident direction and at an azimuth ϕ from their incident electric vector, and then absorbed in a second detector. The concept behind such a polarimeter is the polarization dependency of the differential cross section for Compton scattering

$$\frac{d\sigma}{d\Omega} = \frac{r_0^2}{2}\left(\frac{E'}{E_0}\right)^2\left(\frac{E'}{E_0}+\frac{E_0}{E'}-2\sin^2\theta\cos^2\phi\right) \quad (1)$$

where r_0^2 is the classical electron radius, E_0 the energy of the incident photon, E' the energy of the scattered photon, θ the scattering angle, and ϕ the azimuthal angle relative to the polarization direction. Linearly polarized photons scatter preferentially perpendicularly to the incident polarization vector. Hence, the azimuthal profile $N(\phi)$, in Compton counts recorded per azimuth bin, follows:

$$N(\phi) = S[1 + a_0 cos(2\phi - 2\phi_0)] \quad (2)$$

for a source polarized at an angle PA $= \phi_0 - \pi/2 + n\pi$ and with a polarization fraction PF $= a_0/a_{100}$. The a_{100} amplitude is expected for a 100% polarized source, and depends on the telescope geometry.

2 History of GRB polarization observations

2.1 The past: the RHESSI mission

The RHESSI mission was an observatory dedicated to the study of the Sun. Its spectrometer was composed of nine cooled-down Germanium detectors, which produced Sun images thanks to modulated fine grids. It could measures γ-ray polarization by studying Compton scatterings between two of the Germanium detectors in the 20-2000 keV energy range [2].

In 2002, RHESSI observed a very bright Gamma-Ray Burst, GRB021206, and detected a clear polarized signal [3]. This signal was obtained by subtracting the signal computed by Monte-Carlo simulations for a non-polarized source to the real signal (see figure 1).

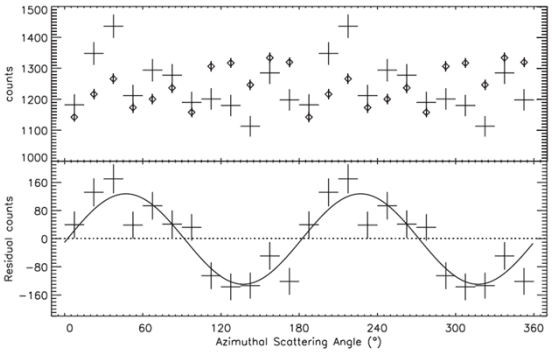

Figure 1: Polarized signal observed with RHESSI from GRB021206 in the 150 keV - 2 MeV energy range. (up) real data (crosses) with simulated non polarized data (points). (bottom) data obtained after subtraction (from [3]).

The data analysis made by Coburn & Boggs was however rediscussed two years later by Rutledge & Fox [4], who demonstrated that most of the "Compton events" used by Coburn & Boggs were not real double events, but single events repeated by the RHESSI on-board electronics. They shown that real double events number was in fact a factor ten below than the ones estimated by Coburn & Boggs, which implied, of course, a lower signal to noise for the Gamma-Ray Burst. Considering this, they show finally that the published polarization signal was in fact dominated by systematics. This example has demonstrated how the Compton polarization data analysis is complex, and that strong efforts should be devolved to the study of systematics, which could mask or even mimic a polarized signal.

2.2 The present : Integral and GAP

Integral observations of GRB041219A polarization

Thanks to its two position sensitive detectors ISGRI [5] (made of CdTe crystals and sensitive in the 15–1000 keV energy band), and PICsIT [6] (made

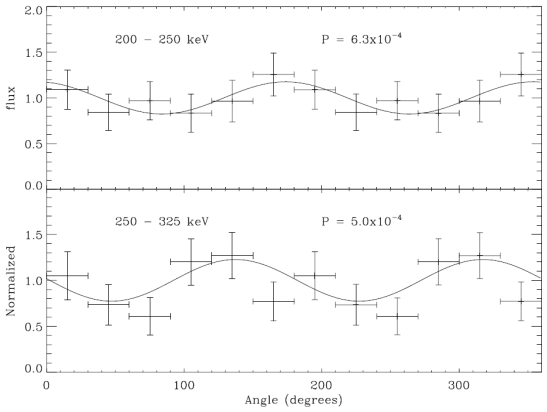

Figure 2: Scatter angle azimuthal distribution of GRB041219A in the 200-250 keV and in the 250-325 keV energy band. These distributions give the source count rate by azimuthal angle of the Compton scattering, and are consistent with a highly polarized signal. The chance probability of a non-polarized signal is reported in each panel. The polarization angles derived from these distributions are consistent within 68° (from [10]).

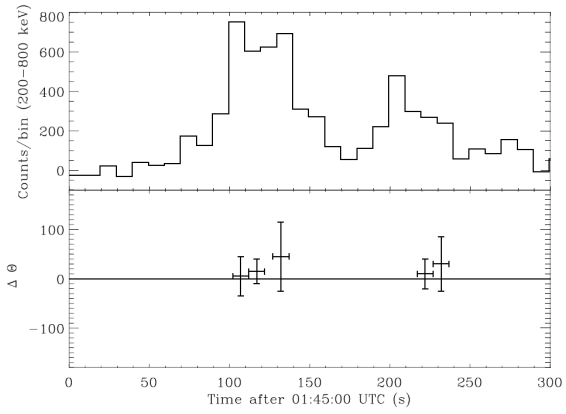

Figure 3: Evolution during the burst duration of the polarimetric angle shift measured between the [200-250 keV] and the [250-325 keV] energy range. The mean value, $21° \pm 47°$, is consistent with zero (from [10]).

of CsI bars and sensitive in the 200 keV–10 MeV energy band), the Integral/IBIS telescope has been also used as a Compton polarimeter to study many compact objects.

As far as GRB are concerned, Götz et al. [8] measure the polarization properties of a bright GRB which occured into the IBIS field of view, GRB 041219A. The procedure to measure the polarization they used is described in Forot el al. [7], and allowed them to control systematic effects and to successfully detect a polarized signal from the Crab nebula. To derive the source flux as a function of ϕ, the Compton photons were divided into 6 bins of 30° as a function of the azimuthal scattering angle. The chance coincidences (i.e. photons interacting in both detectors, but not related to a Compton event), have been subtracted from each detector image following also the procedure described in [7]. The derived detector images were then deconvolved to obtain sky images, where the flux of the source in each azimuthal bin was measured by fitting the instrumental PSF to the source peak. The azimuthal profiles, called hereafter polarigrams, (see Fig. 2) were fitted using a least squares technique with Eq. 2 to derive a_0 and ϕ_0.

Distance to GRB041219A determination

Götz et al. [9] performed deep infra-red imaging using the WIRCam instrument at the 3.6 m Canadian French Hawaiian Telescope (CFHT) at Mauna Kea. Thanks to multi-band ($YJHK_s$) imaging they were able to identify the host galaxy of GRB 041219A, and to constrain its photomeric redshift to $z = 0.31^{+0.54}_{-0.26}$, where the errors are at 1 σ confidence level. This implies a luminosity distance interval of [0.222-5.406] Gpc, assuming standard cosmological parameters ($\Omega_m = 0.3$, $\Omega_\lambda = 0.7$, and $H_0 = 70$ km/s/Mpc).

Constraints on Lorentz Invariance Violation

The scatter angle azimuthal distribution of events coming from GRB 041219A was determined by [10] into two energy band in order to detect a possible polarimetric angle shift with energy, reminiscent of Lorentz Invariant Violation ("LIV") effects [10]. The two bands were chosen to be [200-250 keV] and [250-325 keV] where the source has merely the same signal to noise ratio. In figure 3, we show the measured evolution of the polarimetric angle shift between these two energy bands, along the burst duration. These shifts are all consistent with zero with a mean value of $21° \pm 47°$.

As an exemple, we show also in figure 2 the portion of the GRB light curve where the polarimetric signal was strong, that is starting at 01:47:02 U.T. until 01:47:12 U.T. (P9 interval in [8]). A modulated signal is seen in the two energy bands, corresponding to $PF = 80 \pm 60\%$ for the first band, and $PF = 100 \pm 60\%$ for the second ones. To evaluate the goodness of the fits, the chance probability (see Eq. 2 in [7]) that our polarigrams are due to an unpolarized signal was computed by [10], and reported in Fig. 2. The corresponding polarimetric angles were $PA = 80^{+26}_{-28}$ deg. and $PA = 45^{+38}_{-40}$ deg., that is consistent at the 2σ level. Propagation of errors gives an upper limit of 68° for a possible phase shift.

On general grounds, Lorentz violating operators of dimension $N = n + 2$ modify the standard dispersion relations $E^2 = p^2 + m^2$ by terms of the order of $f_n p^n / M_{Pl}^{n-2}$ where M_{Pl} is the reduced Planck scale ($\approx 2.4\ 10^{18}$ GeV), used as a reference scale since LIV is expected to arise in the quantum regime of gravity. In order to account for the severe limits on LIV, one therefore usually only considers operators of dimension greater or equal to 5 which provide corrections which are tamed by at least one inverse Plank scale.

If we restrict our attention to pure electrodynamics, there is a single term of dimension 5 which gives corrections of order p^3/M_{Pl} and is compatible with gauge invariance and rotational symmetry [11]:

$$\mathcal{L} = \frac{\xi}{M_{Pl}} n^\mu F_{\mu\nu} n^\rho \partial_\rho \left(n_\sigma \tilde{F}^{\sigma\nu} \right) \ , \qquad (3)$$

where n^μ is a 4-vector that characterizes the preferred frame and $\tilde{F}^{\mu\nu} \equiv \frac{1}{2}\epsilon^{\mu\nu\rho\sigma} F_{\rho\sigma}$. The uniqueness of this term makes the analysis somewhat model-independent.

The light dispersion relation is given by ($E = \hbar\omega$ and $p = \hbar k$):

$$\omega^2 = k^2 \pm \frac{2\xi k^3}{M_{Pl}} \equiv \omega_\pm^2 \ . \qquad (4)$$

where the sign of the cubic term is determined by the chirality (or circular polarization) of the photons, which leads to a rotation of the polarization during the propagation of linearly polarized photons. This effect is known as vacuum birefringence.

Since we have the approximative relation:

$$\omega_\pm = |p| \sqrt{1 \pm \frac{2\xi k}{M_{Pl}}} \approx |k| (1 \pm \frac{\xi k}{M_{Pl}}) \ , \qquad (5)$$

the direction of polarization rotates during propagation along a distance d by an angle:

$$\Delta\theta(p) = \frac{\omega_+(k) - \omega_-(k)}{2} d \approx \xi \frac{k^2 d}{2 M_{Pl}} \ . \qquad (6)$$

For GRB041219A, if we set $\Delta\theta(k) = 47°$, derived from the measures we made along the burst duration, and the lower limit luminosity distance reported above of $d = 222$ Mpc $= 6.9\ 10^{26}$ cm, corresponding to z=0.05, we get an upper limit on the vacuum birefringence effect much more constraining than what was derived from experiments on Earth:

$$\xi < \frac{2 M_{Pl} \Delta\theta(k)}{(k_2^2 - k_1^2) d} \approx 0.4310^{-14} \qquad (7)$$

The GAP experiment

The GAP experiment is a Japanese Compton polarimeter launched in 2010, on-board the IKAROS solar sail [12]. It is composed an assembly of two coaxial detectors, made respectively of a plastic scintillator and CsI crystals. Its polarimetric capabilities have been tested on ground in polarized beams to calibrate systematic effects. In 2010, the GRB 100826A Gamma-Ray Burst has been observed by GAP in the 70 to 300 keV energy band. Its modulation was fitted with a Monte-Carlo model of the experiment [12], and a polarized signal was marginally observed with a significance of 2.9 σ (see figure 4).

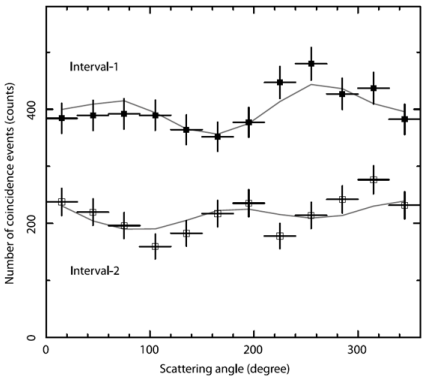

Figure 4: Polarized signal observed with GAP from GRB100826A in the 70 - 300 keV energy range (from [12]).

2.3 The future : POLAR and Astro-H

Today, there is all over the world, only two approved missions, which should fly around 2015, dedicated to the hard X-ray and soft γ-ray observations of polarized light from celestial sources: POLAR and Astro-H. We will describe them below:

The POLAR project

The POLAR telescope is a Swiss led mission dedicated to the Gamma-Ray Burst polarization measurements, to be placed on the Chinese space station Tiangong 2 [13] and supposed to be launched in 2014. This Compton telescope is made by several bars of plastic scintillators read out by photomultiplier as shown in figure 5. Its conception ensures a very wide field of view, and very good polarimetric capabilities ($a_{100} \approx 60\%$, see eq. 2).

The Astro-H SGD polarimeter

ASTRO-H is an international X-ray observatory, which is the sixth in the series of the X-ray observatories from Japan. It is currently planned to be launched in 2014 with an H-IIA rocket from the Tanegashima Space Center, Kagoshima, Japan. Its main scientific objectives are to reveal the large-scale structure and its evolution of the Universe and to understand the extreme conditions in the

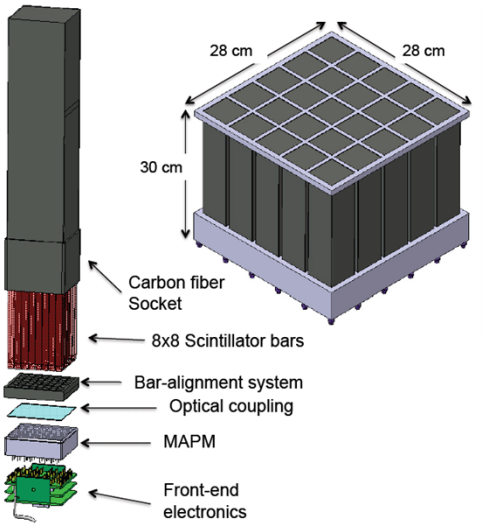

Figure 5: View of the future POLAR mission to be flown on the Chinese Tiangong 2 space station.

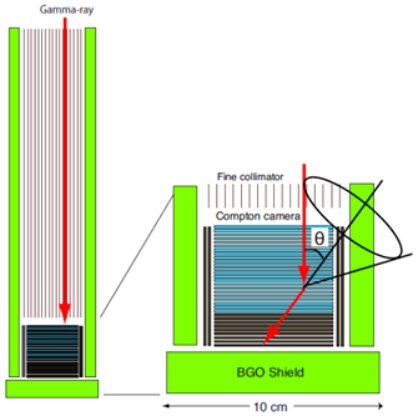

Figure 6: View of the SGD Compton telescope onboard the future Japanese Astro-H mission.

Universe. The mission is approved by JAXA and is currently in its C/D phase. It consists of four instruments including a Compton telescope, which will act as a Compton polarimeter between 5 and 600 keV (the SGD, [14], see figure 6).

The SGD has been heavily tested on ground, and shows very good polarimetric possibilities. However, its rather small fied of view (10°), delimited at high energy (> 300 keV) by BGO collimators, limits its capacities to detect Gamma-Ray Bursts.

3 Conclusions

The measure of hard-X/soft-γ-rays polarization is a powerful tool to investigate the emission mechanisms and geometry of Gamma-Ray Bursts.Also, fundamental physical questions, such as Lorentz Invariance Violation, can be addressed. Several next generation polarimeters (e.g., POLAR, Astro-H) and R&D projects on Compton telescope are on-going all over the world and will complement the present discoveries.

Acknowledgments

ISGRI has been realized and maintained in flight by CEA-Saclay/Irfu with the support of CNES. Based on observations with INTEGRAL, an ESA project with instruments and science data centre funded by ESA member states (especially the PI countries: Denmark, France, Germany, Italy, Switzerland, Spain), Czech Republic and Poland, and with the participation of Russia and the USA.

References

[1] Lei, F., et al. Space Science Reviews **82**, 309 (1997).

[2] Mc Connell M.L. et al., Solar Phys. **210**, 125 (2002).

[3] Coburn W. & Boggs S.E., Nature **43**, 415 (2003)

[4] Rutledge R.E. & Fox D.B., MNRAS **350**, 1288 (2004).

[5] Lebrun, F., Leray, J.P., Lavocat, P., et al., A&A **411**, L141 (2003).

[6] Labanti, C., Di Cocco, G., Ferro, G., et al., A&A **411**, L149 (2003).

[7] Forot, M., et al., *Astrophys. Journal* **688**, L29 (2008).

[8] Götz, D.., et al., *Astrophys. Journal* **695**, L208 (2009).

[9] Götz, D., et al., MNRAS **413**, 2173 (2011)

[10] Laurent P., et al., *Phys. Rev.* D **83**, 121301 (2011).

[11] Myers, R.C. & Pospelov, M. Phys. Rev. Lett. **90**, 211601 (2003).

[12] Yonetoku D., et al., *Astrophys. Journal* **743**, L30 (2011).

[13] Produit N., et al. NIM A **550**, 616 (2005).

[14] Tajima H. et al., Proc. SPIE **7732**, 773216 (2010)

Bulk Lorentz factors and comoving properties of Gamma-Ray Bursts

Lara Nava
APC, AstroParticule et Cosmologie, Université Paris Diderot, CNRS/IN2P3, CEA/Irfu, Observatoire de Paris, Sorbonne Paris Cité, rue Alice Domon et Léonie Duquet, 75205 Paris Cedex 13, France

Abstract

External shocks between the fireball and the surrounding medium are thought to be responsible for the afterglow emission in Gamma-Ray Bursts (GRBs). The peak time of the afterglow bolometric light curve provides an estimate of the initial bulk Lorentz factor Γ_0. For 27 GRBs with known redshift it is possible to estimate Γ_0 from their optical afterglow light curves, while for 4 events Γ_0 can be inferred from high-energy ($> 0.1\,\mathrm{GeV}$) light curves. Typical values are around 140 and 70, depending on the assumption on the density structure of the external medium (homogeneous or wind-like, respectively). The measure of the initial Lorentz factor allows to estimate the properties of the prompt emission in the comoving frame (i.e. in the frame at rest with the relativistic fluid). The comoving energetics, spectral peak energy and luminosity of GRBs have quite narrow distributions. These results provide a general explanation for the existence of the spectral-energy correlations.

1 Introduction

Gamma-Ray Bursts (GRBs) are relativistic sources exploding at cosmological distances. This makes necessary the definition of different reference frames. First, we can define an *observer frame*, (or Earth frame), where fluences, fluxes, observed frequencies and times can be measured. When the redshift of the source is known, it is possible to estimate energetics and luminosities and define the so-called *rest frame* frequencies and durations (i.e., frequencies and durations measured in the frame at rest with the central engine), accounting for cosmological effects. For this reason, the possibility of measuring the spectroscopic redshifts of GRBs opened a new era in the study of these extreme sources. However, still an important correction should be applied. The emitting matter moves at relativistic velocities as seen in the progenitor rest frame and a third reference frame can be defined: the *comoving frame*, i.e., the frame at rest with the relativistic fluid. Large Lorentz factors Γ_0 of the emitting matter imply a strong beaming of the radiation in the rest frame. When Lorentz transformations and Doppler effects are considered, an observer for which the emitting gas moves at small angles with respect to its line of sight sees frequencies enhanced by a factor $\sim \Gamma_0$ and durations reduced by the same factor, with respect to the same quantities measured in the comoving frame.

The most important quantities characterizing the GRB prompt emission are the rest frame peak energy of the νF_ν spectrum (E_{peak}), the isotropic equivalent energetics (E_{iso}) and the isotropic equivalent peak luminosity (L_{iso}). Empirical correlations have been found between these quantities: $E_{peak} \propto E_{iso}^{0.5}$ [1] and $E_{peak} \propto L_{iso}^{0.5}$ [2], which are presently confirmed for a sample of 132 GRB with known spectral properties and redshift. Moreover, for a subsample of 29 events, it is possible to estimate the opening angle of the jet and derive the collimation–corrected energetics of the prompt emission E_γ (i.e., the true energetics emitted by the source) [3, 4]. A tight linear correlation is found ($E_{peak} \propto E_\gamma$) when the ambient medium is assumed to have a wind–like density profile [5].

In this work we estimate Γ_0 from the measure of the peak time of the afterglow light curve [6]. This method has been successfully applied in some cases (e.g. [7]) and more extensively by [8] and [9]. Then, we investigate the presence of correlations between the rest frame quantities (E_{peak}, E_{iso} and L_{iso}) and the bulk Lorentz factor Γ_0. Finally, we present the distributions of the comoving peak energy, energetics and luminosities (E'_{peak}, E'_{iso} and L'_{iso}) and investigate the presence of correlations between these quantities.

2 Estimate of Γ_0

In [9], we collected a sample of 27 GRBs with an initial peak visible in their optical light curves. All these events are classified as long GRBs. We interpreted this peak as the onset of the afterglow emission and computed the Γ_0 factor. The estimate of Γ_0 requires to know the density of the ambient medium where the blast wave expands. We estimate Γ_0 under two different assumptions: i) homogeneous density profile with typical value $n = 3\,\mathrm{cm}^{-3}$ and ii) wind–like density profile (i.e. $n \propto r^{-2}$, as expected in the case of a massive stellar progenitor) with $n = 3 \times 10^{35}\mathrm{cm}^{-1} r^{-2}$. Here r is the shock radius. In the following we refer to these cases as H and W density profiles, respectively. We also assume a γ-ray radiative efficiency of the prompt emission $\eta = 0.2$.

Four GRBs detected by the Large Area Telescope (LAT) on-board Fermi at GeV energies show a peak in their GeV light curves [11], as shown in Fig. 1. We estimate the Lorentz factor of these

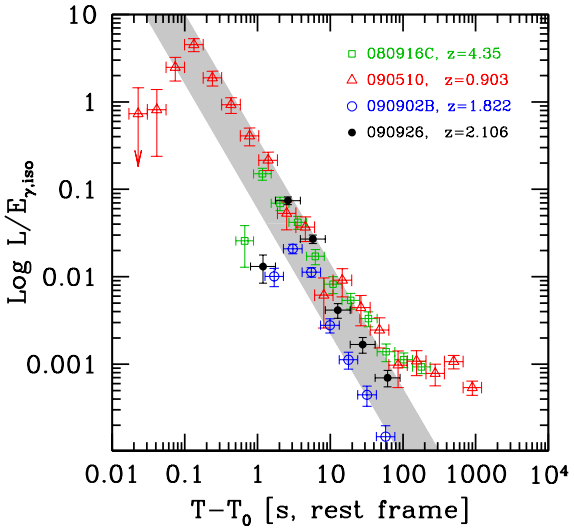

Figure 1: Fermi/LAT light curves (above 0.1 GeV) of the 4 brightest GRBs with redshift detected by LAT. Luminosities are normalized to the total energetics of the prompt emission, measured by the Fermi/GBM. The time is in the rest frame of the sources. Upper limits are at 2σ level. The grey stripe indicates a slope $t^{-10/7}$.

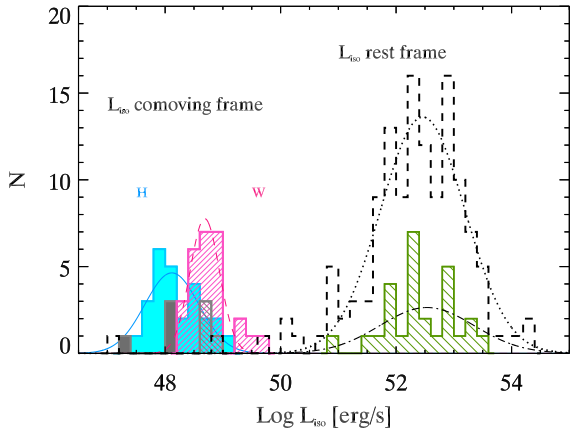

Figure 3: Isotropic luminosity distributions in the rest frame (dashed histogram) for the sample of 132 GRBs with known redshift and constrained E_{peak}. The hatched histogram shows the 31 GRBs of our sample for which we have an estimate of the peak of the afterglow. The beaming-corrected distribution of L'_{iso} is shown by the solid filled histogram and hatched purple histogram for the H and W cases for the 27 GRBs with a peak in the optical light curve. The four bursts with a peak in the GeV light curve are shown for comparison with the hatched and filled grey histograms.

bursts assuming that the emission above 0.1 GeV is synchrotron emission from (forward) external shocks. These events have the smallest peak times in our sample and, therefore, the largest Γ_0 values ($\Gamma_0 \lesssim 10^3$). The interpretation of the GeV emission as afterglow radiation [10, 11, 12], however, is debated. For this reason, the four LAT bursts with peak time measured from the GeV light curve are not considered in our quantitative analysis. We just show them in figures, for comparison with the other bursts.

Among these four LAT bursts there is also the short/hard GRB 090510. However, this burst also shows a clear peak in the optical emission at ∼300 s after the GRB trigger, which questions the afterglow interpretation of the GeV emission. For this burst we estimate Γ_0 also from the peak in the optical light curve and we show the results obtained with both the estimates of Γ_0, which differ by an order of magnitude.

In our sample of 27 events, we find that the average Γ_0 factor is ∼138 in the H case and ∼66 in the W case. In both cases, the distribution is broad, spanning nearly one decade.

3 Correlations and comoving properties

We explore the presence of correlations between the rest frame GRB properties (i.e. the peak energy E_{peak}, the isotropic equivalent energy E_{iso} and luminosity L_{iso}) and the Γ_0 factor. In the upper panels of Fig. 2 we show E_{iso} and L_{iso} (open red circles and filled green squares, respectively) as a function of Γ_0 in both the H and W cases (left- and right-hand panels, respectively). In the bottom panels, instead, we show the peak energy E_{peak} as a function of Γ_0.

We find that there are strong correlations between the spectral peak energy and isotropic energy/luminosity with Γ_0. The slopes of these correlations are rather insensitive to the circum burst profile adopted in deriving Γ_0 (H or W) and are similar for E_{iso} and L_{iso}:

$$E_{iso} \propto \Gamma_0^2 \qquad L_{iso} \propto \Gamma_0^2 \qquad (1)$$

A roughly linear correlation exists between E_{peak} and Γ_0:

$$E_{peak} \propto \Gamma_0 \qquad (2)$$

We estimate the comoving properties by applying the beaming corrections (see [9] for the derivation of the corrections that should be applied to move from the rest frame to the comoving frame):

$$E'_{peak} = \frac{3E_{peak}}{5\Gamma_0} \qquad E'_{iso} = \frac{E_{iso}}{\Gamma_0} \qquad L'_{iso} = \frac{3L_{iso}}{4\Gamma_0^2}$$

We found that there is a reduction of the dispersion of the distribution of the peak energy from the rest frame to the comoving one. In the comoving frame E'_{peak} clusters around ∼ 6 keV and ∼ 3 keV in the H and W cases, respectively, with dispersions of

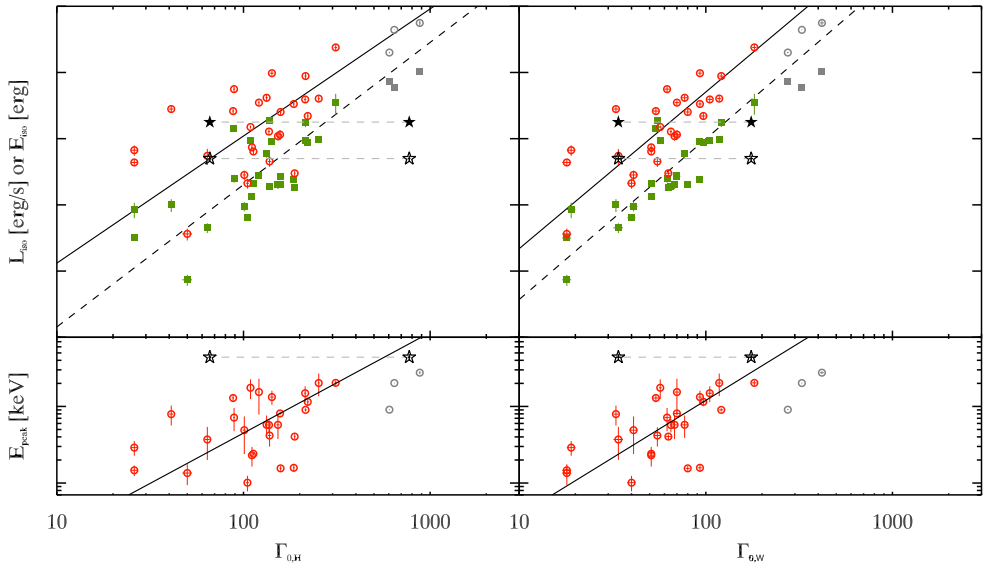

Figure 2: Top panels: E_{iso} (open circles) and L_{iso} (filled squares) as a function of Γ_0 for the 31 GRBs in our sample in the H case (left panel) and W case (right panel). The solid (dashed) line in both panels show the fit to the E_{iso}–Γ_0 (L_{iso}–Γ_0) correlation for the sub-sample of 27 GRBs with peak in the optical light curve (open red circles and filled green squares). The three GRBs with peak in the GeV light curve are shown with the grey symbols and are not included in the fits. The short GRB 090510 with both a peak in the GeV and a delayed peak in the optical is shown by star symbols connected by the dashed (grey) line. Bottom panels: peak energy E_{peak} for the H case (left-hand panel) and W case (right-hand panel) as a function of Γ_0. The solid line is the best-fitting correlation.

nearly one decade, i.e. narrower than the dispersion of E_{peak}. Similar results are found for the energetics: the distributions of E'_{iso} are wide, but there is a reduction of the dispersion from the rest to the comoving frame. On average, the comoving frame $E'_{iso}\sim$ 1–3$\times10^{51}$erg, both in the H and W case. Interestingly, we find a strong clustering of the comoving frame distribution of L'_{iso} (Fig. 3). For the H case we find an average $L'_{iso}\sim 10^{48}$ erg s^{-1} with a small dispersion (0.47 dex), while when using the Γ_0 computed in the wind density profile (W) case we find an almost universal value of $L'_{iso}\sim 5\times10^{48}$ erg s^{-1} with a dispersion of less than 1 order of magnitude around this value.

4 Discussion and conclusions

In Fig. 4, we show the rest frame E_{peak}–E_{iso} (left panel) and E_{peak}–L_{iso} (right panel) correlations (updated here with 132 GRBs up to 2011 May). We also show the comoving frame E'_{peak} and E'_{iso} (left panel) and E'_{peak} and L'_{iso} (right panel) for the GRBs of our sample with an estimate of Γ_0 in the W case (similar results are found when Γ_0 is estimated assuming a homogeneous density profile). The 27 GRBs with a peak in the optical are shown with the cyan filled squares, while the three long and one short GRBs with a peak in the GeV light curve are shown with the filled grey squares and filled star, respectively.

As we discussed in the previous section, E'_{peak} and L'_{iso} are contained in a narrow range. This means that all bursts emit their radiation at a characteristic frequency in their comoving frame and with a characteristic luminosity, irrespective of their bulk Lorentz factor. In the comoving frame, we do not find any correlation between E'_{peak} and L'_{iso}: as shown in Fig. 4, these two quantities occupy a quite clustered region of the plane. Since, as we found in the previous section, $E_{peak}\propto\Gamma_0$ and $L_{iso}\propto{\Gamma_0}^2$ (see Eq. 1 and Eq. 2), moving from the comoving to the rest frame obviously introduce a correlation between the rest frame quantities in the form $E_{peak}\propto L_{iso}^{0.5}$. With a similar argument, also the correlation $E_{peak}\propto E_{iso}^{0.5}$ can be explained. This implies that the empirical correlations found in the rest frame are the result of different Γ_0 factors. Indeed, bursts with the lowest Γ_0 lie in the bottom part of the correlations, while at the upper end there are bursts with the largest Γ_0. The E_{peak}–E_{iso} and E_{peak}–L_{iso} correlations could be a sequence of Γ_0 factors.

In this scenario, the E_{peak}–E_γ correlation can also be explained if the jet opening angle inversely correlates with the bulk Lorentz factor $\theta_{jet}\propto\Gamma_0^{-1/2}$, leading to:

$$\theta_{jet}^2\Gamma_0 = const \qquad (3)$$

If we assume this relation, we find, for the collimation corrected energy E_γ:

$$E_\gamma = \theta_j^2 E_{iso} \propto \Gamma_0 \propto E_{peak} \qquad (4)$$

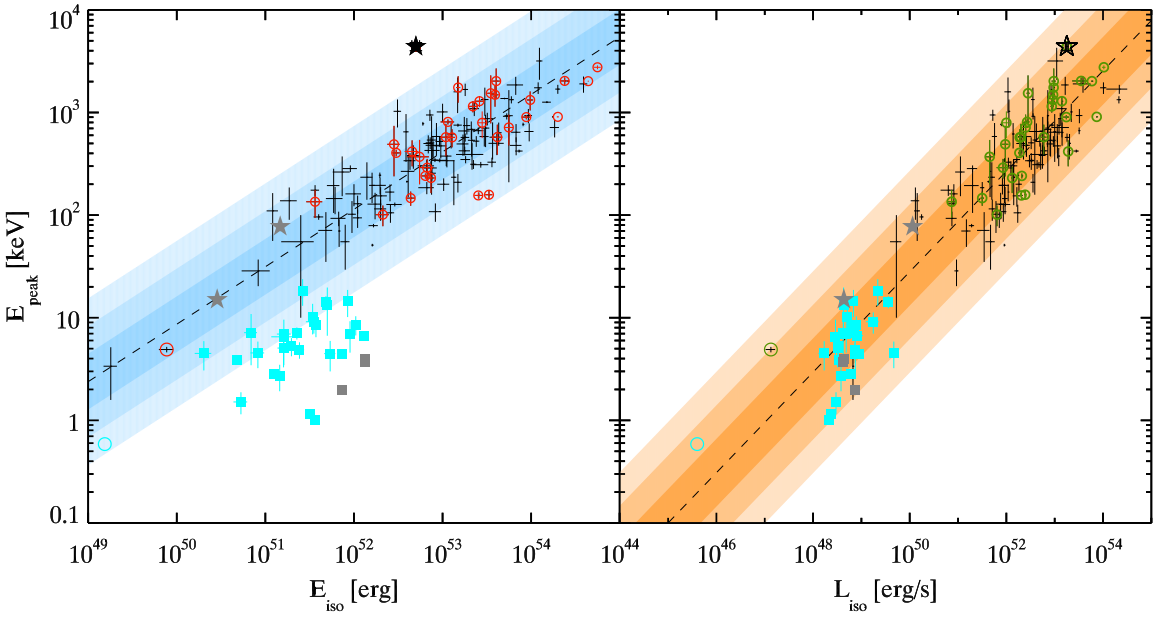

Figure 4: Left: E_{peak}–E_{iso} correlation in the rest frame (crosses and red circles) for 132 GRBs with z and fitted E_{peak} updated up to 2011 May. Right: E_{peak}–L_{iso} correlation with 131 GRBs. In both panels, the best-fitting correlation is shown by the dashed line and its 1σ, 2σ, 3σ scatters are shown by the shaded region. The comoving frame E'_{peak} and E'_{iso} (left) and E'_{peak} and L'_{iso} (right) of 30 GRBs [red open circles (left-hand panel) and green open circles (right-hand panel)] in our sample with an estimate of the Γ_0 factor are shown with the filled cyan square symbols (27 events with peak time in the optical light curve) or grey filled square (the three long GRBs with a peak in the GeV light curve). The short GRB 090510 is also shown with a star symbol and the low-luminosity GRB 060218 (with $\Gamma_0 \sim 5$) is shown with an open circle.

An important consequence is that, in the comoving frame, the collimation corrected energy E'_γ becomes constant:

$$E'_\gamma = \theta_j^2 \frac{E_{iso}}{\Gamma_0} = constant \qquad (5)$$

This allows us to re-interpret the clustering of L'_{iso} as a consequence of the constant E'_γ:

$$L'_{iso} \sim \frac{E'_\gamma}{T'_{90}\theta_j^2} = \frac{E'_\gamma}{T_{90}\theta_j^2\Gamma_0} = constant \qquad (6)$$

In other words, in the comoving frame, each burst emits the same amount of energy at the same characteristic peak frequency, irrespective of its bulk Lorentz factor. For larger Γ_0 the emitting time in the comoving frame is longer (by a factor Γ_0 if the observed T_{90} is the same), so the comoving luminosity is smaller. But since the jet opening angle is also smaller (for larger Γ_0), the isotropic equivalent luminosity turns out to be the same.

References

[1] Amati, L., Frontera, F., Tavani, M., et al. A&A **81**, 390 (2002)

[2] Yonetoku, D., Murakami, T., Nakamura, T., Yamazaki, R., Inoue, A. K., Ioka, K. *Astrophys. Journal* **935**, 609 (2004)

[3] Ghirlanda, G., Ghisellini, G., Lazzati, D. *Astrophys. Journal* **331**, 616 (2004)

[4] Ghirlanda, G. AIPC **579**, 1111 (2009)

[5] Nava, L., Ghisellini, G., Ghirlanda, G., Tavecchio, F., Firmani, C. A&A **471**, 450 (2006)

[6] Sari, R. & Piran, T. *Astrophys. Journal* **641**, 520 (1999).

[7] Molinari, E., Vergani, S. D., Malesani, D., et al., A&A **13**, 469 (2007).

[8] Liang, E.-W., Yi, S.-X., Zhang, J., Lu, H.-J., Zhang, B.-B., Zhang, B., *Astrophys. Journal* **2209**, 725 (2010).

[9] Ghirlanda, G., Nava, L., Ghisellini, G., Celotti, A., Burlon, D., Covino, S., Melandri, A. MNRAS **483**, 420 (2012)

[10] Kumar, P., Barniol Duran, R., MNRAS **75**, 400 (2009)

[11] Ghisellini, G., Ghirlanda, G., Nava, L., Celotti, A. MNRAS **926**, 403 (2010)

[12] Ghirlanda, G., Ghisellini, G., Nava, L., A&A **7**, 510 (2010)

Properties of Galaxies hosting Gamma-Ray Bursts

Sandra Savaglio
Max Planck Institute for extraterrestrial Physics, Giessenbachstr., 85741, Garching, Germany
email: savaglio@mpe.mpg.de

Abstract

Due to their extreme luminosities, gamma-ray bursts (GRBs) are routinely detected in hostile regions of galaxies, nearby and at very high redshift. Thus, they are important cosmological probes. During recent years, the investigation of galaxies hosting GRBs demonstrated their connection with star-formation activity. However, the link to the total galaxy population is still poorly understood, due to the small-number statistics: less than 50 hosts have been studied in detail over a total of 270 GRBs with spectroscopically measured redshifts. Moreover, at present, mainly low-redshift ($z < 2$) hosts were observed, leading to a typical galaxy with low luminosity, low metallicity and active star-formation. Nevertheless, recent studies hint towards different properties at $2 < z < 4$, where some hosts are massive, metal rich and show red colors due to high dust content. Understanding the reasons for these apparently contradicting results is the goal of on-going projects. Finally, the most distant population ($z > 4$) is basically unconstrained due to lack of detections.

1 Introduction

Long duration gamma-ray bursts (GRBs[1]) are associated with the core collapse of massive stars ($M > 40$ M$_\odot$; [1]) and, as such, are located preferentially in regions experiencing immediate star formation [2]. GRBs are so luminous that they can shine through highly absorbed galaxies that at high redshift are difficult to reach using conventional background QSO techniques. Today, more than 270 GRB redshifts are measured, among which the most distant spectroscopically-confirmed object known, at $z = 8.2$ [3, 4].

It is often claimed that GRB hosts are special galaxies, characterized by low chemical enrichment and intense star formation [2, 5]. However, high metallicities have been measured in several GRB host galaxies ([6], and references therein) suggesting that intense star formation might be alternatively the dominant factor producing a GRB [7, 8].

Cosmic heavy element enrichment is nowadays measured in different ways, probing the properties of the interstellar medium (ISM) in substantially different galaxy populations. This is illustrated in Fig. 1. For a long time, absorption lines detected in QSO spectra (damped Lyman-α systems, DLAs) were easily accessible, because QSOs are bright and relatively common, up to the highest redshift. More recently, the 8-m class telescopes allowed the detection of emission lines from the hot ISM in UV bright galaxies up to $z \sim 2$. However, only GRBs can probe all components of a galaxy simultaneously, from which the chemical enrichment in both cold and hot ISM can be investigated. It is now possible, observing one class of targets, to measure galaxy parameters with absorption and emission lines, in bright and faint objects (Fig. 1).

[1] From now on, we consider long GRBs only and call them simply GRBs

2 The nature of high-z GRB host galaxies

The reputation that depicts GRB hosts as metal poor galaxies is not always justified. It is on average true at redshift $z < 1.5$, but at high redshift ($z > 2$) metallicities measured with absorption lines in GRB afterglow spectra display a large dispersion. Two extreme examples are compared in Fig. 2. The host of GRB 090926A at $z = 2.1062$ is gas rich and metal poor, about 1/100 times the solar value [9]. The host of the more distant GRB 090323 ($z = 3.57$) has super-solar metallicity, and a peculiar strong double absorption system separated by ~ 700 km s^{-1} [10]. High-z GRB host galaxies are not necessarily similar to a typical dwarf galaxy in the nearby universe [11].

The pair absorbers in the spectrum of the afterglow of GRB 090323 suggests that interactions may play a role in the formation of massive stars at high redshift. The idea is related to the detection of a high fraction of $z > 1.5$ double absorbers with small velocity separations along GRB sightlines [12, 13, 10]. The fraction of double absorbers compared to the total population of 53 GRBs at $z > 1.5$ is 9.4%, almost three times higher than the fraction in QSO-DLAs (which probe random galaxies). Interestingly, this fact reminds the detection of several z > 2 supernovae with very massive ($M \sim 40 - 250$ M$_\odot$) progenitors associated with interacting (double-peaked Lyα emission) Lyman break galaxies (LBGs) [14].

Before a more quantitatively statement will be derived, another indication is provided by the disturbed morphologies or galaxy pairs associated with several GRBs [15, 16, 17]. One example is GRB 050820A (Fig. 3). This GRB at $z = 2.613$ happened between galaxy A and B, which are at the same red-

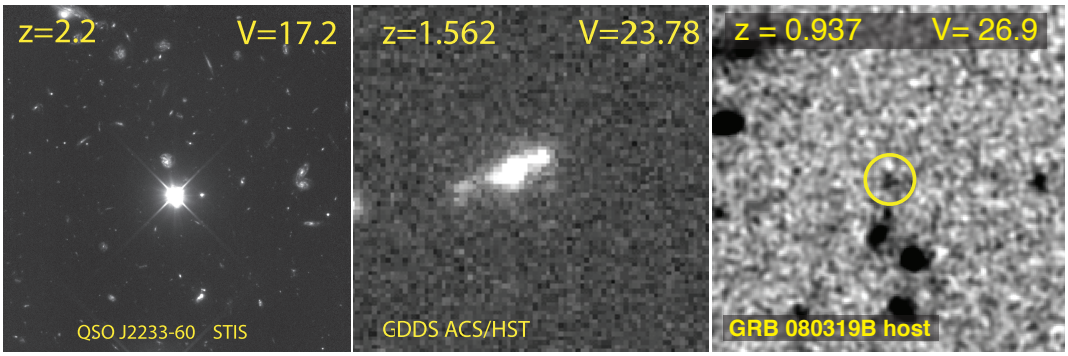

Figure 1: In the recent history of astrophysics, the chemical enrichment of the ISM in the distant universe has been estimated by observing different targets (QSOs, field galaxies or GRBs). On the left, in the center and on the right the image of a high-z QSO, a bright star-forming galaxy and a faint GRB host, whose apparent brightness can differ by several orders of magnitude.

shift of the GRB and are separated by about 15 kpc. The interaction hypothesis is also supported by the higher fraction of galaxy mergers found in the past than today [19]. The merging triggers immediate star formation episodes or bursts, that make them favorable sites for high-z GRBs and luminous supernovae.

3 Most massive GRB hosts

The importance of the investigation of GRB host galaxies has become evident because of the connection of these objects with the most active, observationally hostile, and remote regions of the universe. As already mentioned, at $z > 2$ some GRB hosts are metal rich, others are massive, dusty, and highly star forming [20, 21, 22], in contrast with the low-metallicity, low-mass hosts commonly found at $z < 1.5$. Dusty, massive and star-forming galaxies can be very bright in the sub-millimeter. These are called sub-millimeter galaxies (SMGs). Early sub-mm investigations of some GRB hosts has shown very promising results about the connection with SMGs [23]. However, latest results of a larger $z < 1$ sample has not confirmed what was probably a combination of small number statistics and misidentification for at least one galaxy [24].

One possible explanation for this missing GRB-SMG population is indicated by the star-formation rate density (SFRD) of the universe, in Fig. 4. Gray filled circles are measurements from field galaxies [25], while red diamonds and blue circles are derived from GRBs by two different teams [26, 27] (but see also, among others, [28, 29]), suggesting that the traditional technique using UV bright galaxies might not give the most complete census of high-z star formation rate. On the other hand, low-z sub-mm galaxies (SMGs) [30] can only account for at most 20% of the total SFRD, and the contribution is even less for ultra-luminous infrared galaxies

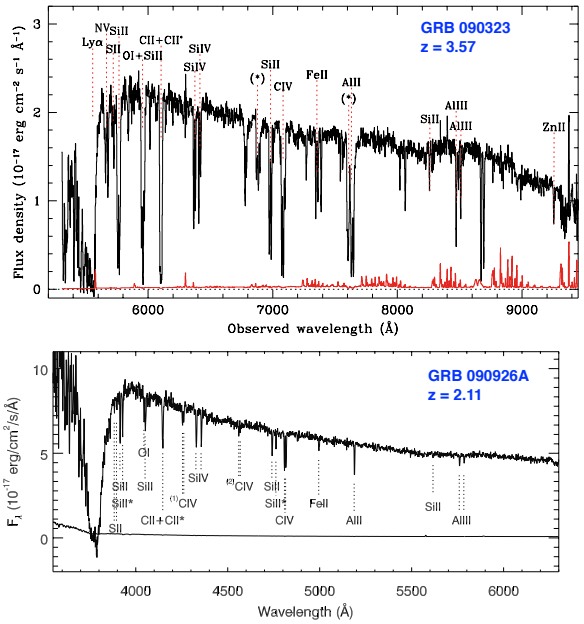

Figure 2: Comparison of two very different GRB afterglow spectra at high redshift, probing the interstellar medium in galaxies. Bottom and top panels, GRB 090926A at $z = 2.11$ [9] and GRB 090923 at $z = 3.57$ [10], respectively.

(ULIRGs) [31]. However, the steep increase with redshift of the SFRD probed by SMGs indicates that the gap might be partly bridged at $2 < z < 4$. If this is going to be the case, we will probably find that SMGs constitute an important fraction of GRB host galaxies at those redshifts.

4 Conclusions

The impact of GRB host galaxies on cosmology is still limited by the small number statistics. Fig. 5, showing the histogram of GRBs per redshift bins and the comparison with the cosmic SFRD derived from UV and Hα bright galaxies [25], suggests that

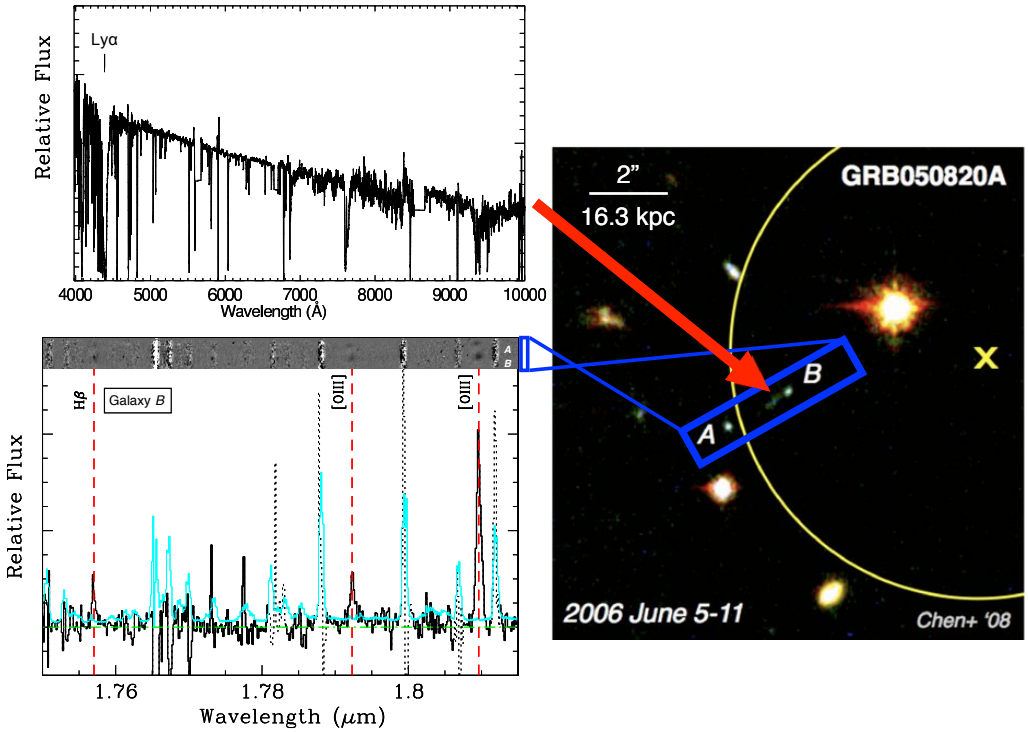

Figure 3: *Right panel*: the field of GRB 050820A. Its location is indicated by the red arrow [15]. *Upper left panel*: the spectrum of the afterglow from which a redshift $z = 2.613$ was measured [18]. *Lower left panel*: 2D Spectrum of galaxy A and B (indicated in the right image), and below the 1D spectrum of galaxy B. Both galaxies are at the same redshift of the GRB [15].

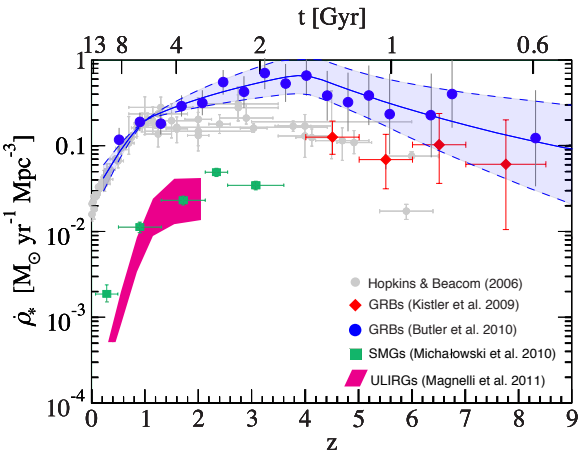

Figure 4: The star formation rate density as a function of redshift. Gray circles are measurements from field galaxies [25]. Red diamonds [26] and blue circles [27] are derived from GRBs, respectively. Green squares are measurements from low-z SMGs [30]. The magenta area is the contribution from ULIRGs [31].

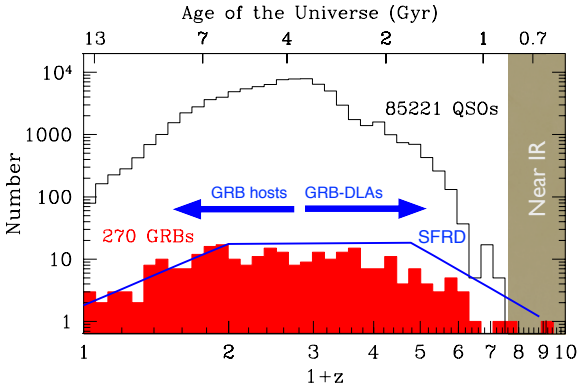

Figure 5: Histograms of the observed number of GRBs and QSOs per redshift bin (in units of $\log(1+z)$). The number of GRBs increases from $z = 0$ to ~ 1, it is steady up to $z \sim 3$, then it decreases down to zero at $z \sim 9$. At low and high z, redshifts are mainly measured front the host galaxy or the DLA detected in the optical afterglow, respectively. Dust (mainly at $z = 1 - 3.5$) and flux limits (for $z > 3.5$) affects our high-z detections. We compare this behavior with the schematic SFRD derived from field galaxies [25], scaled to match the observed $z < 1$ GRB histogram. If we assume that the $z < 1$ GRB histogram is proportional to the SFRD, and that many GRBs are missed for higher redshift, this comparison suggests that a fraction of the SFRD is missed by galaxy surveys.

a fraction of the SFRD at $z > 1$ is missed by most popular surveys. One important step forward is the multi-wavelength (from X-ray to radio) approach, which can statistically quantify the importance of red galaxies associated with dark GRBs. Exploitation of the long wavelength regime is now possible thanks to the capabilities of new ground-based telescopes (SCUBA-2, APEX, ALMA, ATCA) and space missions (Spitzer, Herschel, WISE). This will ultimately establish whether some high-z GRB hosts are connected to dusty sub-millimeter galaxies. At even lager redshifts, the situation will probably be different again, given the difficulty of finding GRB hosts, even through deepest search [32, 33].

Acknowledgments

I express my gratitude to the worksop organizers for the kind hospitality and the outstanding scientific program they put together.

References

[1] Heger, A., et al. *Astrophys. Journal* **591**, 288 (2003)

[2] Fruchter, A., et al. *Nature* **441**, 463 (2006)

[3] Salvaterra, R., et al. *Nature* **461**, 1258 (2009)

[4] Tanvir, N., et al. *Nature* **461**, 1254 (2009)

[5] Levesque, E., et al. *Astron. Journal* **140**, 1557 (2010)

[6] Savaglio, S. *IAU Symposium* **279**, 212 (2012)

[7] Fynbo et al. *Astrophys. Journal* **683**, 321 (2008)

[8] Pontzen et al. *Mon. Not. R. Astr. Soc.* **402**, 1523 (2010)

[9] Rau, A., Savaglio, S., Krühler, T., et al. *Astrophys. Journal* **720**, 862 (2010)

[10] Savaglio, S., et al. *Mon. Not. R. Astr. Soc.* **420**, 627 (2012)

[11] Thuan, T. X., Izotov, Y. I., & Lipovetsky, V. A. *Astrophys. Journal* **477**, 661 (1997)

[12] Fynbo, J., et al. *Astrophys. Journal* **633**, 317 (2005)

[13] Page, K. L., et al. *Mon. Not. R. Astr. Soc.* **400**, 134 (2009)

[14] Cooke, J., et al. *Mon. Not. R. Astr. Soc.* **403**, 1020 (2010)

[15] Chen, H.-W. *Mon. Not. R. Astr. Soc.* **419**, 3039 (2012)

[16] Krühler, T., et al. *Astro. & Astrophysics* **in press**, arXiv:1203.1919 (2012)

[17] Thöne, C., et al. MNRAS **414**, 479 (2011)

[18] Fynbo, J. P. U., et al. *Astrophys. Journal* **185**, 526 (2009)

[19] Bluck, A. F. L., et al. *Astrophys. Journal S.* **747**, 34 (2012)

[20] Hunt, L., et al. *Astrophys. Journal* **736**, L36 (2011)

[21] Krühler, T., et al. *Astro. & Astrophysics* **534**, A108 (2011)

[22] Rossi, A., et al. *Astro. & Astrophysics* **545**, A77 (2012)

[23] Michałowski, M. J., et al. *Astrophys. Journal* **672**, 817 (2008)

[24] Michałowski, et al. *Astrophys. Journal* **755**, 85 (2012)

[25] Hopkins, A. M., & Beacom, J. F. *Astrophys. Journal* **651**, 142 (2006)

[26] Butler, N. R., Bloom, J. S., & Poznanski, D. *Astrophys. Journal* **711**, 495 (2010)

[27] Kistler, M. D., et al. *Astrophys. Journal* **705**, L104 (2009)

[28] Elliott, J., et al. *Astro. & Astrophysics* **539**, A113 (2012)

[29] Robertson, B. E., & Ellis, R. S. *Astrophys. Journal* **744**, 95 (2012)

[30] Michałowski, M., Hjorth, J., & Watson, D. *Astro. & Astrophysics* **514**, A67 (2010)

[31] Magnelli, B., et al. *Astro. & Astrophysics* **528**, A35 (2011)

[32] Basa, S., et al. *Astro. & Astrophysics* **542**, A103 (2012)

[33] Tanvir, N. R., et al. *Astrophys. Journal* **754**, 46 (2012)

All-Sky monitor in hard X-rays and soft gamma-rays with Wide-Field Gamma-Ray Telescope Gammascope

V.V. Bogomolov, V.I. Galkin, A.F. Iyudin, O.V. Morozov, S.I. Svertilov
Extreme Universe Laboratory, Skobeltsyn Institute of Nuclear Physics, Lomonosov Moscow State University, 1(2), Leninskie gory, GSP-1, Moscow 119234, Russian Federation

Abstract

The main purpose of Gammascope is to study astrophysical transient phenomena such as cosmic Gamma-Ray Bursts (GRBs), by means of simultaneous all-sky observations in hard X-rays and soft gamma-rays (0.02 2.0 MeV), and optical band. In particular, the GRB study is one of the main goals of modern astrophysics. While being one of the most powerful phenomena in the Universe, GRBs are not well understood up to now for lack of insight on their central engine. Nevertheless, GRBs give us also an independent cosmological test and could be used for studing the very early stages of the Universe evolution.

The experiment main feature is the possibility of simultaneous observations of GRBs in gamma-rays and optical. The Gammascope project is designed to detect at the same time the optical and gamma emission at the moment of the explosion. This instrument represents a new step in that it is expected to obtain gamma-ray images of large areas of the sky, significantly improving the accuracy of GRB localisation in the gamma energy range.

1 Scientific objectives

The main goal of this project is to develop such an all-sky monitor to study astrophysical transient phenomena such as GRBs, supernovae and novae, outbursts in X-ray binaries and pulsars, active galactic nuclei variability during simultaneous all-sky observations in hard X-rays and soft gamma-rays (0.02 – 2.0 MeV), and optical band. The investigation of these phenomena is very timely in view of fundamental problems of modern physics such as the origin and evolution of the Universe, the nature of dark matter and dark energy, the space-time structure and matter properties in very high electromagnetic and gravitational fields. In particular, the study of GRBs is one of the main goals of modern astrophysics. Being one of the most powerful events in the Universe, GRBs are not well understood up to now for lack of adequate insight on their central engine. Nevertheless,GRBs give us also an independent cosmological test and could be used for studing the very early stages of the Universe evolution.

The experiment main feature is the possibility of simultaneous observations of GRBs in gamma-rays and optical. Hitherto, mainly the so-called afterglow, i.e. the response of the surrounding medium to an explosion in the GRB source, was observed in optical. The Gammascope instrument is constructed to detect contemporaneously the optical and gamma emission of the GRB at the instant of explosion. From this point of view, it continues the line of research of the Lomonosov mission, which is devoted to the multi-wavelenght study of GRB prompt emission. However, the Gammascope is qualitatively a new step because it is expected to obtain gamma-ray images of large sky areas, and it will significantly improve the accuracy of the GRB localisation.

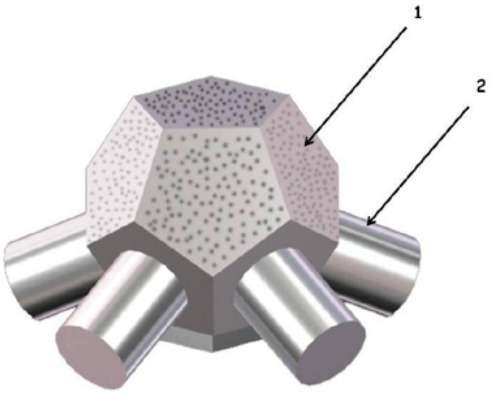

Figure 1: The general view of a wide field-of-view hard X-ray monitor: 1 – marks the coding mask element; 2 – marks one of the PSD modules.

2 Composition of Gammascope

The hard X-ray monitor consists of the wide-field gamma-ray telescope (WFGRT) sensitive to photon energies from ∼10 keV up to 1.0 MeV, and a number of wide-field optical cameras (WFOC). WFGRT (see Fig. 1) is an arrangement of identical units of position-sensitive detector (PSD) modules and a coded mask. It could also include a separate electronic unit. The coded mask should be as similar to spherical as possible. In practice, it is made as the arrangement of six separate identical pentagonal elements, which are mounted on a special construction of a dodecahedronal shape.

The WFGRT position-sensitive detector consists of the 6 modules, which are placed on the bot-

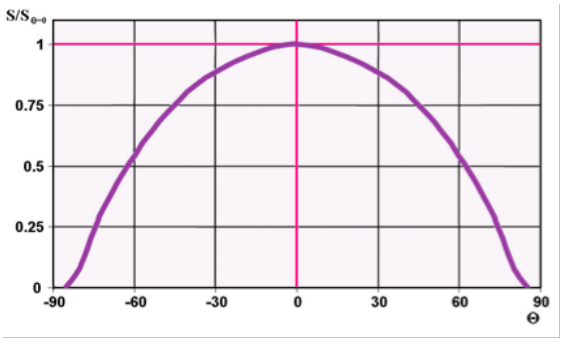

Figure 2: The field-of-view of the all-sky monitor Gammascope.

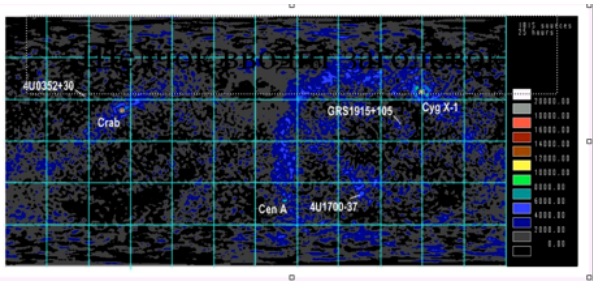

Figure 3: Reconstructed image of the Galactic plane for one orbit exposure data of "Gammascope" collected in a survey-mode. Point sources with quite different X-ray luminosity are well separated and identified in the map.

tom surface of a special dodecahedron construction in such a way that each PSD module is opposite to a coded mask pentagonal element. In this way, observations of a given part of the sky become possible by PSD corresponding coded mask element combination, which in combination cover the whole semi-sphere. Each PSD module is based on the NaI(Tl)/CsI(Tl) phoswich detector. The NaI(Tl) consists of a large number (100) of relatively small pixels (2.0×3.0 cm^3) with CsI(Tl) crystals placed under the pixels and used as the active shield from the locally produced gamma-quanta.

In the optimal case six WFOCs should be co-aligned to each PSD – coded mask element combination. Thus, the WFOC field (2020°) will be totally covered by the larger field of WFGRT PSD module (60° FWHM), see Fig. 2. Due to its very high cost, the number of WFOCs may in fact be smaller than the number of PSD modules – 3 or 4.

The instruments effective area and exposure time should be maximized for detection of the weakest sources, the maximal number of GRBs etc. The value T · S (i.e. the product of the instruments FOV solid angle, total time of experiment T and effective area S)could be used as the universal parameter of the experiments survey sensitivity [1]. The minimal detectable fluxes for the proposed coded mask all-sky monitor were calculated for T = 1 year, = 2 sr and S = 500 cm^2 with the use of the expected background level estimated from the data of the GRIF experiment onboard the Mir orbital station [2]. The survey sensitivity of the proposed all-sky monitor is about 2×10^{-4} cm^{-2} s^{-1} MeV^{-1} in the 0.1-1.0 MeV energy range. This is of the same order of the survey sensitivity of the IBIS/INTEGRAL instrument near 100 keV and the COMPTEL/CGRO instrument at 1 MeV.

3 Instrument status

To present the design documentation of separate modules and units has been elaborated, but the update of the NaI(Tl) pixels by faster scintillating crystals of $LaBr_3$:Ce needs to be taken into consideration.

Mathematical modelling of gamma-quanta interaction in the detector units was performed and an image reconstruction technique was elaborated by means of a software allowing to obtain the sky map in the equatorial co-ordinates in scanning mode.

To optimize the image reconstruction algorithm, the instrument response to a point-like source with given intensity was modelled for different source positions. To estimate the opportunities of sky map reconstruction by the summing of exposures, the scanning of the sky by the instrument field of view (FOV) due to the spacecraft motion was modelled for realistic experimental conditions. As a result, the possibility of discrimination between nearby sources, as well as weak source detection capability, and the background from 10 times more intense bright objects was confirmed. Fig. 3 clearly shows that in the case of continue scanning of the sky by the instrument FOV, it is possible to separate the different sources in the Galactic Centre.

As a result of this simulation, the possibility of spatial resolution of the tightly placed point sources with a luminosity span up to a factor 10 was confirmed for the real background conditions of low-orbital satellite. Note that the energy coverage of Gammascope is well suited to measure the peak energy of the GRB prompt emission spectrum, which makes this hard X-ray monitor a valuable addition to the UFFO-100 instrumental suite, able to provide an estimate of the redshift of detected GRBs using peak energy-z relation.

Moreover, an analysis of possible adaptations of the main instrument units and modules to the space experiment conditions was performed. This means proposals on the PSD module construction and electric circuits as well as on the telemetric control of the instrument. The necessary output data volume was estimated.

The main parameters of the monitor Gammas-

cope are given in Table 1.

Total mass of the instrument Mass of the detector	160 kg 130 kg
Applied power	95 W
Data flow per day	32 Mb
Geometry factor	0.3 m^2sr
Angular resolution	2-3 deg
Energy range	0.05-1.0 MeV
Energy resolution (661keV line)	15 %
Effective area	500 cm^2
Sentitivity (106 s observation time)	30 mCrab

Table 1:

References

[1] Kudryavtsev, M.I., Svertilov, S.I., Bogomolov, V.V, & Bogomolov A.V. Adv. Space Res. **22**, 1057 (1998)

[2] Kudryavtsev, M.I., Svertilov, S.I., Bogomolov, V.V & Bogomolov A.V. Adv. Space Res. **22**, 1053 (1998)

Development of an electron tracking Compton camera for both balloon and future satellite experiments for MeV gamma-ray astronomy

Toru Tanimori (on behalf of SMILE project)
Department of Physics, Graduate School of Science, Kyoto University, Kyoto 606-8502, Japan

Abstract

In order to explore MeV gamma-ray astronomy, we have developed the Electron Tracking Compton Camera (ETCC). By measuring the track of a recoil electron event by event, ETCC measures the direction of each gamma-ray as a small arc (not circle), which strongly suppresses the leakage of background to the Field of View (FoV). Also the kinematical check for the angle between a recoil electron and a scattered gamma ray is a good tool for background rejection. ETCC onboard a satellite would be a good candidate for an all sky MeV gamma-ray survey of a wide energy region in the 0.1-100 MeV range, with several ten times better sensitivities than COMPTEL. We already carried out a balloon experiment with a small 10 cm cube ETCC (Sub-MeV gamma ray Imaging Loaded-on-balloon Experiment: SMILE-I) in 2006. We are now constructing a 30 cm cube ETCC to catch gamma-rays from the Crab and terrestrial gamma-ray bursts in the Polar region using a long duration balloon flight around the North Pole in 2014 (SMILE-II project). Terrestrial gamma-ray bursts are generated by relativistic electron precipitation from the radiation belt in the Polar region. Furthermore I stress the unique capability of ETCC to find high z Gamma-Ray Bursts (GRBs) beyond z $>$ 10, in particular long duration GRBs of over 10^3 s, which are expected for Population-III stars.

1 Introduction

Although MeV gamma-ray astronomy remains unexplored, observations in the sub-MeV and MeV regions are expected to provide unique science such as line gamma rays from radioisotopes by nucleosynthesis, electron-positron annihilation lines, and neutron capture lines from solar flares and black holes. Furthermore continous gamma ray emissions from pulsars, active galactic nuclei (AGN), and in particular gamma ray bursts (GRB) are promising targets for future astronomy.

However, observation of such low-energy gamma rays is very difficult due to the complex physical process of Compton scattering in the detector and large backgrounds produced in the satellite and atmosphere (albedo). Actually COMPTEL in the 1990s was well known to suffer from huge background contamination, and consequently only about 30 celestial persistent objects were found in the MeV region [1], whereas EGRET detected 270 sources [2] and Fermi found 1451 sources above 100 MeV during the first 11 months [3]. COMPTEL rejected most of the background using the time of flight between forward and backward detectors, and then detected 30 objects. Thus COMPTEL showed the necessity of a robust background rejection for the detection of more than 100 objects. As it is well known, most of the MeV gamma rays are emitted as continous spectra, and hence the background rejection method is absolutely needed. Here we explain the balloon experiment project (SMILE project [4]) with the new detector having such background rejection ability.

2 ETCC and SMILE-Project

2.1 Electron Tracking Compton Camera (ETCC)

We (Cosmic-ray Gamma Group, Kyoto University) developed an electron-tracking Compton camera (ETCC) as shown in Fig.1 [5, 6]. The ETCC consists of a 3D electron tracker, and a pixel scintillator for measurement of the energy and absorption point of scattered gamma rays. By measuring the recoil electron tack, the direction of an incident gamma ray is determined not by a circle but by an arc for each photon. Furthermore, the measurement of the residual angle between the scattering gamma ray and the recoil electron (α in Fig.1) provides a kinematical background rejection tool. In addition, dE/dx of the recoil electron easily lets us distinguish the stopping electron in the ETCC from background particles such as cosmic muons and neutrons. These new tools are quite efficient in rejecting backgrounds for continous gamma ray emissions.

As an electron tracker, we have developed a micro time projection chamber (μ-TPC, Fig. 1) using a micro pixel chamber named μ-PIC. Gd_2SiO_5:Ce was adopted as a scintillator for the pixel scintillator arrays (PSAs) where the pixel size is $6 \times 6 \times 13$ mm^3, and one array consists of 8×8 pixels. The average energy resolution is approximately 11% (FWHM) for 662 keV. GSO is known as a good scintillator for space use due to its non-hygroscopicity and radiation hardness. We have already confirmed our detector concepts by means of ground-based experiments [6].

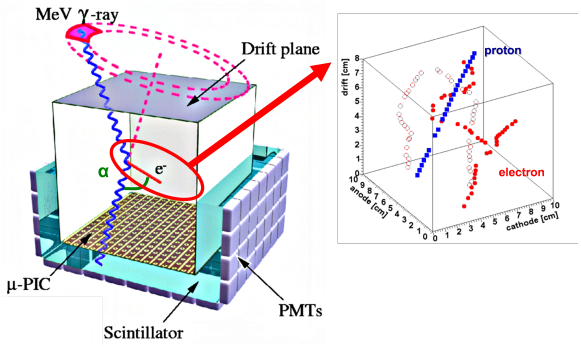

Figure 1: Structure of ETCC and measured 3D tracks of electrons and protons.

2.2 SMILE-project

We have carried out the balloon experiments: "Sub-MeV gamma ray Imaging Loaded-on-balloon Experiment", called SMILE in order to validate the capability of the ETCC for MeV astronomy. The first step was an operation test at balloon altitudes and the certification of the background rejection power by the observation of the diffuse cosmic and atmospheric gamma rays. In 2006, a small size ETCC with a $10 \times 10 \times 15$ cm^3 Xe-based TPC and 33 PSAs of GSO (SMILE-I) [7] was developed as SMILE-I ETCC, and launched from the JAXA Sanriku Balloon Center. During 3 hours observation, we obtained 420 downward gamma-ray events from about 2×105 triggered events, which was nearly equal to the expected number of 400 events from Geant4 simulation. By obtaining the growth curve, fluxes of the diffuse cosmic and atmospheric gamma rays were obtained, which were consistent with those of other past observations [7]. Thus, the ETCC of SMILE-I succeeded to observe gamma rays at balloon altitude while rejecting other particles, the details of which are described in [7]. This result addressed that a future ETCC having a larger $50 \times 50 \times 50$ cm^3 volume would provide a sensitivity 10 times better than that of COMPTEL in the sub-MeV region.

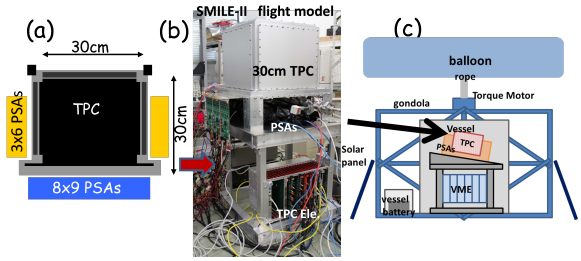

Figure 2: (a) side view of SMILE-II ETCC; (b) photo of SIMLE-II flight model under construction; (c) concept of SMILE-II Instrument.

Following SMILE-I, we are constructing SMILE-II (Fig.2) to verify the imaging ability of ETCC by observing of the Crab [8]. In order to detect Sub-MeV gamma rays from the Crab during 5 hours at a 5 σ level at Japan latitude, a 30 cm cubic ETCC has been developed as shown in Fig. 2. We have started the collaboration with EISCAT [9], since SMILE-II is expected to detect the terrestrial gamma-ray burst emitted from relativistic electron precipitation (REP) in the polar region. High energy electrons are accelerated in the radiation belts up to several MeV, and precipitated on the pole regions. A Bremsstrahlung gamma-ray burst by REP was first observed in 1996 at Kiruna [10], and then a few ten REP events were observed in Antarctica by the MAXIS balloon experiment [11]. Because the ETCC loaded on SMILE-II has an angular resolution of several degrees and a large Field of View (FoV) of 3 str, SMILE-II will observe weaker REP bursts than MAXIS. In addition, we expect to resolve the effect of REP on the generation and circulation of ozone and NOx in the upper atmosphere thanks to the collaboration with EISCAT [12], which measures the radio waves from secondary electrons and ions generated by REP. From the Kiruna base, a circum-polar long duration balloon flight of about 2 weeks (= 366 hours) is managed by the Swedish Space Cooperation. This long duration flight will be useful not only for the REP observation, where the detection of about 150 REP events is expected by SMILE-II, but also for astronomical observation. As it is well known, cosmic-ray background in the polar region is unluckily about 5 times higher than in Japan, but several hundred hours observation will provide good statistics of > 10 σ for the Crab. In addition, such a long duration flight will give us a chance to detect some celestial outbursts such as GRBs, as mentioned in the next section.

3 Science of SMILE

3.1 Gamma-rays from REP

In the Polar region, Bremsstrahlung gamma rays from the REP will be observed simultaneously during the observation of celestial targets due to the large FoV. Fine tracking of charged particles in the TPC also provides the detection of fast neutrons from solar proton precipitation. By measuring the energy and the depth of gamma rays in the atmosphere from the observed image, the precipitation position will be determined. A REP burst similar to that of 1996 would be detected at a level higher than 20 σ. Furthermore, weaker precipitation events down to $\sim$1/10 the atmospheric background can be measured by imaging observations, which will provide the quantitative estimate of the rate of REP. Based on MAXIS experiment results,

several REP events per day will be detected by SMILE-II. In addition, ETCC can image fast neutrons generated by high energy proton precipitation simultaneously.

We propose a ground-based measurement campaign, including the EISCAT radars, all-sky cameras and photometers, as well as suitably located VLF receivers in support of the SMILE-II balloon campaign. The balloon experiment would be launched from Kiruna in 2014 corresponding to the solar maximum activity. We also collaborate with Japanese ERG satellite [13] and Russian RELEC satellite [14].

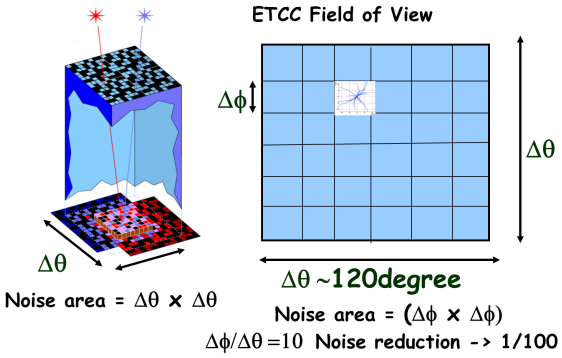

Figure 3: Scmematic explanation of FoV for real imaging trigger. Left is trigger region of Code Mask ($\Delta\theta \times \Delta\theta$, and right is a trigger region ($\Delta\phi \times \Delta\phi$) of ETCC in the wide FoV $\Delta\theta \times \Delta\theta$.

3.2 Gamma-Ray Bursts

In addition, gamma-ray bursts are a good target for ETCC in future satellite observations since ETCC can implement a real imaging similar to that of an optical telescope by detecting the direction of each gamma ray [15]. Real gamma-ray imaging will be quite important for triggering weak and long GRBs, which are expected for high-z GRBs. First of all, the reduction of the background is crucial for triggering weak and long GRBs. A simple way is a real imaging detecting the direction of each X-ray or gamma ray with a large FoV of > 1 str as shown in Fig. 3. Although a real imaging with a large FoV is actually impossible for X-rays, ETCC could satisfy it for 80keV photons and above where the Compton process is dominant. High-z GRBs are expected to emit predominantly photons between 10 keV and a few MeV, and thus Compton imaging could be available. However, conventional Compton imaging hardly identifies the point source from several hundred photons while simultaneously rejecting huge backgrounds. On the other hand, ETCC could identify the direction of the gamma-ray source from several tens of photons, and simultaneously reject the background quite efficiently as mentioned in Sec. 2.1.

Since the cosmic background photon flux ($>$ 100 keV) is ~ 0.2 ph cm^{-2} s^{-1} str^{-1}, the expected photon flux in a $4^\circ \times 4^\circ$ region of the sky is only $\sim$ 8 ph ($>$ 100 keV) during 10^2 s for a satellite of the size of ETCC with a 100 cm^2 effective area, of which the gas volume is $\sim 1 \times 1 \times 0.5$ m^3 (hereafter we call it sETCC). Thus, the real imaging of gamma rays could generate the trigger on the small frame of $\sim 4^\circ \times 4^\circ$ in the 3 str FoV. Such a triggering method dramatically reduces the background down to near a several hundreds of that in 1str FoV. The photon limit for triggering GRBs at a 8 σ level is $\sim$ 60 photons in the small frame. Due to the low background level, this trigger scheme can accumulate events up to 10^4 s or more, which is also a powerful tool to increase the figure of merit of the trigger. In particular, this long accumulated trigger looks effective for the dilation effect on high-z GRBs and Population-III GRBs [16, 18], which are expected to appear with a quite long duration of 10^4 s.

Usually the figure of merit is proportional to $\sqrt{}$ (effective area times triggering duration) $/\sqrt{}$ (FoV of the triggering frame). We find that the sETCC is superior by $\times$ 10 times to the typical Coded Mask (CM) detector, where we use a typical CM detector with an effective area 5000 cm^2 ($>$ 15 keV), triggering duration 10 s, and FoV for triggering $100^\circ \times 100^\circ$ and the sETCC with 100 cm^2, 100 s, and $4^\circ \times 4^\circ$, respectively. Point accuracy of sETCC is estimated at $\sim 0.2^\circ$ and $\sim 0.5^\circ$ for 300 and 50 photons, respectively. A typical CM detector needs $\sim 10^4$ X-ray photons for pointing, which corresponds to several 100 gamma-rays ($>$ 100 keV) at the ETCC energy band based on the typical spectrum of GRBs. For short GRBs with T90 $<$ 10 s, ETCC sensitivity looks similar to a typical CM detector. However, for longer duration GRBs, s-ETCC could accumulate gamma-rays during the whole T90 period, and its sensitivity would be improved dramatically. For 10^3 sec long duration GRBs, sETCC could detect weaker GRBs by a factor of several 10 over a CM detector. High-z GRBs with z$>$ 10 and $E_{iso} > 10^{52}$ erg are estimated to be detected with about 1000 gamma-ray photons by accumulating most gamma rays during their long duration. Details are described elsewhere [15].

Since T90 of higher z GRBs (z $>$ 10) is expected to be longer than 10^2 s, it seems difficult that its peak flux can exceed 0.1 ph/cm^2/s, which is the detection limit of the future large area coded mask detectors. On the other hand, ETCC is a real imaging detector such as an optical telescope, and hence

a longer exposure increases the sensitivity. Thus, ETCC has a unique potential to detect long duration GRBs such as population-III GRBs of which the duration time exceeds 10^3 s. If several GRBs with duration longer than 10^3 s were detected, this would be a significant direct evidence of the existence of POP-III stars.

In a two week flight around the North Pole, about 10 GRBs would appear in the FoV of the ETCC. For typical GRBs ($> 10^{-6}$ erg/cm^2 in the 10-100 keV energy region), several tens of photons (> 100 keV) are expected to hit the ETCC. Thus, in several balloon fights in the North Pole, we will be able to clarify the feasibility of the imaging trigger of the ETCC for GRBs.

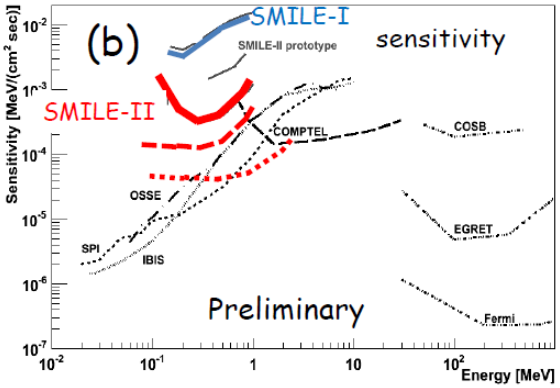

Figure 4: Expected detection sensitivity of SMILE-II for an observation time of 10^6 s at a significance of 3 σ with the comparison to previous observations. The solid and dashed red lines represent the sensitivity of SMILE-II with a 0.5 cm^2 effective area and including the improvement of the tracking in TPC, respectively. The dotted red line is for a 40 cm cube SMILE with $\times 10$ cm^2 effective area

4 Perspective

We have developed an ETCC as a next-generation MeV gamma-ray telescope. To study the feasibility of future observations with satellites, we carry out the SMILE balloon experiment project. SMILE-I was launched in 2006. Now we are preparing SMILE-II with a 30 cm cubic ETCC for the observation of the Crab. SMILE-II is required to increase the detection area over 50 times that of SMILE-I, and we have already developed such an ETCC. In particular, a new reconstruction method for the tracking has greatly improved the detection efficiency. The expected sensitivity of SMILE-II including feature improvement is shown in Fig.4, where it is indicated that the sensitivity below 500 keV will be improved by the new reconstruction method [19]. However, note the deterioration of the efficiency in the higher energy region above 1 MeV which is mainly due to the penetration of higher energy recoil electrons from the TPC. Recently we proposed to set the plastic scintillator inside the TPC to capture the recoil electrons, which enables us to keep a moderate efficiency up to 10 MeV [20]. In addition, above 10 MeV the TPC will be a good tracker of pair creation in the multi MeV region [21]. Thus, ETCC has the potential to cover the energy range from 0.1 to 100 MeV. At present, we are carrying out the SMILE-II project with a long duration balloon flight around the North Pole planned for 2014 (and in 2013 a one day flight for checking SMILE-II). In this flight, detection of terrestrial gamma-ray bursts in the Polar region is another important science goal for the SMIEL-II project. In addition, such a long flight will give us a chance to clarify the feasibility of the imaging trigger for long duration GRB in ETCC.

Acknowledgments

The SMILE project is carried out by the Cosmic-ray gamma Group, in the Dept. of Physics, Kyoto University [4]. North-pole balloon experiment is collaborated with Dr. M.Yamauchi (IRF), Dr. S.Arvelius (Lulea Tech. Univ) and Dr. E.Turunen (EISCAT). SMILE-II was supported by a Grant-in-Aid for Scientific Research and a Grant-in-Aid from the Global COE program "Next Generation Physics, Spun from Universality and Emergence" the Department of Physics and Astrophysics, Kyoto University, from the Ministry of Education, Culture, Sports, Science and Technology (MEXT) of Japan. Also it was supported by the joint research program of the Solar-Terrestrial Environment Laboratory, Nagoya University and the National Institute of Polar Research through General Collaboration Projects no 23-3.

References

[1] Schönfelder, V., et al. *Astronomy & AstrophysicsSupp.* **143**, 145 (2000).

[2] Hartman, R.C., et al. *Astrophys. Journal Supp.* **123**, 79 (1999).

[3] Abdo, A.A., et al. *Astrophys. Journal Supp.* **188**, 405 (2010).

[4] http://www-cr.scphys.kyoto-u.ac.jp/research/MeV-gamma/en/index.html.

[5] Tanimori, T., et al. Astron. Rev. **48**, 263 (2004).

[6] Takada, A., et al. *Nucl. Instrum. Methods* A **546**, 258 (2005).

[7] Takada, A., et al. *Astrophys. Journal* **733**, 13 (2011).

[8] Takada, A., et al. 20th ESA Sympo. on European Rocket and Balloon Programmes , 567 (2011).

[9] EISCAT, http://www.eiscat.se/.

[10] Foat, E.E., et al. Geophys. Res. Lett. **25**, 4109 (1998).

[11] Millan, R.M., et al. Geophys. Res. Lett. **29**, 2194 (2002).

[12] Turunen, E., et al. Journal of Atm. & Solar-Terr. Phys. **71**, 1176 (2009).

[13] http://gemsissc.stelab.nagoya-u.ac.jp/erg/.

[14] http://smdc.sinp.msu.ru/elana/experiments/relec/index.html.

[15] Tanimori, T. AIP Conf. Proc. **1279**, 220 (2010).

[16] Meszaros, P., Rees, M.J. *Astrophys. Journal* **715**, 967 (2010).

[17] Toma, K., et al. *Astrophys. Journal* **731**, 127 (2011).

[18] Suwa, Y., Ioka, K.*Astrophys. Journal* **726**, 107 (2011).

[19] Tanimori, T., et al SPIE Proc. **8443**, 10 (2012).

[20] Takada, A., et al. IEEE Conf. Pub. **NP3.M-I00**, 1215 (2011).

[21] Ueno, K., et al. *Nucl. Instrum. Methods* A **628**, 158 (2010).

Acknowledgments

The Workshop *"Gamma-Ray Bursts: Probing the Science Progenitors and their Environment"* and the present Proceeding volume represent part of the scientific activity performed by the Extreme Universe Laboratory. The Organizing Committee would like to acknowledge the support of the Russian Federation under the Contract N 11.G34.31.0076 d.d. 01.11.2011 for scientific research in the field of "Studies of an epoch of repeated ionization of young Universe by means of registration of gamma-ray bursts and their afterglow during space experiments (observable cosmology)".